International Journal of Solids and Structures 50 (2013) 957–975

Contents lists available at SciVerse ScienceDirect

International Journal of Solids and Structures

journal homepage: www.elsevier.com/locate/ijsolstr

Solidification–microprestress–microplane (SMM) theory for concrete at early age: Theory, validation and application

Giovanni Di Luzio [a], Gianluca Cusatis [b,*]

[a] Department of Structural Engineering, Politecnico di Milano, Piazza Leonardo Da Vinci 32, 20133 Milan, Italy
[b] Department of Civil and Environmental Engineering, A125 Tech Building, Northewestern University, Evanston, IL, USA

ARTICLE INFO

Article history:
Received 6 August 2012
Received in revised form 1 November 2012
Available online 21 December 2012

Keywords:
Concrete
Early age
Cracking
Shrinkage
Creep
Relative humidity
Temperature

ABSTRACT

This paper presents a new constitutive model describing the mechanical behavior of concrete at early age and beyond. This model, entitled solidification–microprestress–microplane (SMM) model, amalgamates the microplane model and the solidification–microprestress theory and takes into account all the most significant aspects of concrete behavior, such as creep, shrinkage, thermal deformation, and cracking starting from the initial stages of curing up to several years of age. Age-dependent viscoelastic behavior under variable hygro–thermal conditions is described according to the solidification–microprestress theory. Cracking/damage behavior is modeled through an age-dependent microplane model, in which the model parameters are assumed to be dependent on an aging variable evolving with the extent of early-age chemical reactions (hydration, silica-fume reaction, etc.) and temperature. Calibration and validation of the model is performed by the numerical simulations of the age-dependent response of sealed and unsealed specimens subject to a variety of loading conditions and/or drying. Comparison with experimental data shows that the SMM model can reproduce well the interplay of shrinkage, creep, and cracking phenomena during curing and drying.

1. Introduction

A reliable constitutive model for concrete at early age must be able to reproduce creep, shrinkage, hygro–thermal phenomena, as well as linear and non-linear deformations from the onset of hardening and beyond. In addition, it must take into account complex phenomena such as (1) creep under variable hygro–thermal conditions during concrete aging; (2) autogenous and drying shrinkage; (3) evolution with age of mechanical properties (i.e. compressive and tensile strength, fracture energy, etc.). In the present work a novel model, which, in the initial stages of development, was presented in recent conferences (Di Luzio et al., 2010a; Di Luzio and Cusatis, 2012), is formulated by amalgamating and extending the microprestress–solidification theory (Bažant and Prasannan, 1989a,b; Bažant et al., 1997a,b, 2004) and the updated M4 microplane model (Bažant et al., 2000; Bažant and Di Luzio, 2004; Di Luzio, 2007).

At early age, deformations can be caused by shrinkage, which develops in a cement-based materials as moisture is lost to the environment or by self-desiccation, and by thermal expansion due to the heat produced during early-age chemical reactions (among others, see Neville (1997), Khan et al. (1997), and Wittmann et al. (2009)). Moreover, cracking or strain-softening damage may occur due to external and internal restraints which contrast volumetric expansions and contractions caused by hydration heat and shrinkage (Cusson and Hoogeveen, 2007). External restraints include structural restraints, e.g. when the volume is not free to dilate due to contact with a subbase or a previously cast structure or when concrete is cast around rigid corners or around rigid inserts. Internal restraints are caused by gradients in the dilation of the material or by rigid parts of the material itself, e.g. shrinkage cracking around aggregates. Typical structures sensitive to these problems include bridge decks, pavements, and all massive structures, such as large foundations, large columns, thick walls, dams.

In the present study, the visco-elastic behavior of concrete is modeled through (1) the solidification theory (Bažant and Prasannan, 1989a,b), where the solidifying constituent (the hardened cement gel) is assumed to be age-independent and the chemical aging is interpreted as a volume growth of the solidifying constituent related to a reaction degree. This approach greatly reduces the number of material parameters in the modeling of aging creep and it allows a unique identification from test data of the age-dependent moduli of Kelvin (or Maxwell) chains typically used to model concrete creep. (2) The microprestress theory (Bažant et al., 1997a,b, 2004) assumes that drying creep, long-term creep and variation of relative humidity and temperature can be explained by the same physical theory, resting on the idea of relaxation of self-equilibrated stresses (microprestresses) created in the solid

* Corresponding author.
E-mail address: g-cusatis@northwestern.edu (G. Cusatis).

0020-7683/$ - see front matter © 2012 Elsevier Ltd. All rights reserved.
http://dx.doi.org/10.1016/j.ijsolstr.2012.11.022

nano-structure of the cement gel by microscopic volume changes of various chemical species during hydration and by the imbalance of chemical potentials among the four phases of pore water (vapor, capillary, adsorbed, and hindered adsorbed phases).

In the proposed formulation, the microplane model is used to characterize the material properties of young concrete, such as tensile and compressive strength, fracture energy, damage, and nonlinear (cracking) strains. The microplane model, initially formulated by Bažant and coworkers (Bažant and Gambarova, 1984; Bažant et al., 2000; Bažant and Di Luzio, 2004; Di Luzio, 2007), is a general three-dimensional constitutive law able to reproduce accurately strain softening in tension and compression as well as the reverse from softening to hardening upon confinement. The microplane model has been calibrated and validated extensively with comparison to experimental data. The updated M4 version of the microplane model as improved by Di Luzio (2007) is adopted in this study and modified to account for the evolution of mechanical properties at early age. It is worth noting here that other version of the microplane model (Ožbolt et al., 2001; Bažant and Caner, 2005) could be adopted as well and extended to early age in a similar way.

The early-age evolution of material properties require preliminary calculation of hydration degree, humidity and temperature fields which can be obtained through the chemo–thermo–hygral (CTH) model (Di Luzio and Cusatis, 2009a,b). This model is capable of simulating moisture transport and heat transfer in ordinary and high-performance concrete by taking into account explicitly the coupled effect of cement hydration, SF pozzolanic reaction, and silicate polymerization. The model was calibrated and validated extensively on the basis of experimental data available in the literature (Di Luzio and Cusatis, 2009b).

Many theoretical and computational studies on the behavior of concrete at the early age can be found in the literature. However, no one of them has a comprehensive formulation capable of simulating the phenomena mentioned previously. Among others, Ulm and Coussy (1995, 1996) proposed a thermo–chemo–mechanical model for the prediction of deformation and cracking accounting for strength growth through chemo–plastic coupling within the theory of elasto-plasticity. In the aforementioned studies, however, the effect of creep and relative humidity were not considered. Cervera et al. (1999a,b) formulated a coupled thermo–chemo–mechanical model for the behavior of concrete at early ages. This model is capable of simulating the observed phenomena of hydration, aging, damage, and creep based on an appropriate thermodynamic framework. The short- and long-term mechanical behavior is modeled by means of a viscoelastic damage model that accounts for the aging effects using the micro-prestress/solidification theory. However, in this model the effect of the relative humidity is not considered. Lackner and Mang (2004) proposed a chemo–mechanical model for early-age cracking of concrete in which the effect of relative humidity is neglected. Gawin et al. (2006a,b) developed a hygro–thermo–chemo–mechanical model of concrete at early ages which comprehensively accounts for the aging and hygro–thermal coupling but lacks a comprehensive constitutive law for cracking/damage in tension and unconfined compression and for hardening plasticity for confined compression.

The formulation highlighted in the next section overcomes most the limitations of models currently available in the literature and it is characterized by the following innovative aspects:

1. For the first time in the literature the considered microplane model, a general three-dimensional constitutive equation for concrete, is extended to account early age phenomena.
2. Aging effects are accounted for in a unified fashion through the concept of "reaction degree" which was formulated by the authors in an earlier publication dealing with the hygro–thermal aspects of early-age behavior (Di Luzio and Cusatis, 2009a,b) but never used in the contest of a comprehensive constitutive equation for concrete mechanical behavior.
3. A new aging law dependent on the more general reaction degree concept as opposed to the earlier adopted equivalent time is proposed for the solidification theory.
4. The model is calibrated and validated extensively with reference of several sets of data.

2. Multi-physics formulation

The formulation proposed hereinafter consists of a multi-physics framework that simulates: (1) the mechanical behavior of concrete, including visco-elasticity (creep/relaxation), cracking and damage, hygro–thermal deformations (shrinkage, swelling, thermal expansion/contraction); (2) heat transfer due to environmental temperature variations (heating/cooling) and internal heat generation by exothermic chemical reactions; (3) moisture variation and moisture diffusion associated with environmental exposure (drying/wetting) and internal (chemical) water consumption; (4) the evolution of chemical reactions (cement hydration, silica-fume reaction, etc.) occurring at early-age in concrete and, more generally, in cementitious composites; and (5) aging, that is the evolution of the mechanical and hygro–thermal material properties from the time of casting to the completion of early-age chemical reactions.

2.1. Mechanical behavior

In this study, the classical assumption of Cauchy's continuum is adopted to describe the mechanical behavior of concrete at early-age. The governing equations expressing the concepts of equilibrium and compatibility, can be then written as

$$\nabla \cdot \boldsymbol{\sigma} + \boldsymbol{b} = \mathbf{0} \quad \text{and} \quad \boldsymbol{\epsilon} = \frac{1}{2}\left(\nabla \boldsymbol{u} + \nabla^{\mathrm{T}} \boldsymbol{u}\right) \tag{1}$$

where $\boldsymbol{\sigma}$, $\boldsymbol{b}$, $\boldsymbol{\epsilon}$, $\boldsymbol{u}$, are the stress tensor, the body force vector, the strain tensor, and the displacement vector, respectively. Note that thereinafter bold Greek letters are used either to represent tensors or their vectorial contraction according to Kelvin notation: $\boldsymbol{\sigma} = [\sigma_{11}\ \sigma_{22}\ \sigma_{33}\ \sqrt{2}\sigma_{23}\ \sqrt{2}\sigma_{13}\ \sqrt{2}\sigma_{12}]^{\mathrm{T}}$ and $\boldsymbol{\epsilon} = [\epsilon_{11}\ \epsilon_{22}\ \epsilon_{33}\ \sqrt{2}\epsilon_{23}\ \sqrt{2}\epsilon_{13}\ \sqrt{2}\epsilon_{12}]^{\mathrm{T}}$. Also, in Eq. (1) and hereinafter the direct dependence of all variables on time is dropped for better readability of the equations.

The boundary value problem in Eq. (1) can be solved when appropriate (essential and/or natural) boundary conditions are prescribed and a constitutive equation is formulated. The constitutive equation formulated in this paper is based on the assumption that the strain additivity holds. One can write

$$\dot{\boldsymbol{\epsilon}} = \dot{\boldsymbol{\epsilon}}^{i} + \dot{\boldsymbol{\epsilon}}^{v} + \dot{\boldsymbol{\epsilon}}^{f} + \dot{\boldsymbol{\epsilon}}^{d} + \dot{\boldsymbol{\epsilon}}^{s} + \dot{\boldsymbol{\epsilon}}^{t} \tag{2}$$

where $\dot{\boldsymbol{\epsilon}}$ is the total strain rate, $\dot{\boldsymbol{\epsilon}}^{i}$ is the instantaneous strain rate; $\dot{\boldsymbol{\epsilon}}^{v}$ is the viscoelastic strain rate; $\dot{\boldsymbol{\epsilon}}^{f}$ is the purely viscous strain rate; $\dot{\boldsymbol{\epsilon}}^{d}$ is the inelastic strain rate due to cracking and damage; and $\dot{\boldsymbol{\epsilon}}^{s}$, $\dot{\boldsymbol{\epsilon}}^{t}$ are hygral and thermal strains caused by variations of relative humidity and temperature, respectively. It is worth noting here that the strain additivity assumption, largely adopted in the concrete mechanics literature (Bažant and Planas, 1997), is equivalent to the adoption of the rheological model depicted in Fig. 1, which, due to the series coupling, lead to a constant stress state in the different elements of the chain.

2.1.1. Microprestress–solidification theory

The instantaneous strain rate, $\dot{\boldsymbol{\epsilon}}^{i}$, is the strain increment appearing immediately after the application of a stress increment, $\dot{\boldsymbol{\sigma}}$, and can be expressed as $\dot{\boldsymbol{\epsilon}}^{i} = q_1 \mathbf{G}\dot{\boldsymbol{\sigma}}$. At typical room temperatures and

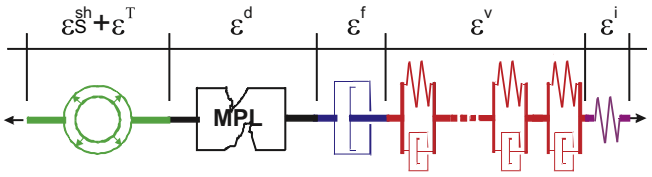

Fig. 1. Schematic representation of the constitutive model.

for saturation condition, parameter q_1 (in MPa^{-1}) is age independent as demonstrated by Bažant and Baweja (1995). In addition, if one assumes that material isotropy is preserved during the visco-elastic evolution of the material and that Poisson's ratio, ν, is time independent (Bažant and Planas, 1997), then matrix $\mathbf{G}$ is constant:

$$\mathbf{G} = \begin{bmatrix} 1 & -\nu & -\nu & 0 & 0 & 0 \\ -\nu & 1 & -\nu & 0 & 0 & 0 \\ -\nu & -\nu & 1 & 0 & 0 & 0 \\ 0 & 0 & 0 & 2(1+\nu) & 0 & 0 \\ 0 & 0 & 0 & 0 & 2(1+\nu) & 0 \\ 0 & 0 & 0 & 0 & 0 & 2(1+\nu) \end{bmatrix} \tag{3}$$

The value $\nu = 0.18$ will be used in all numerical simulations presented in this paper.

The viscoelastic strain rate, $\dot{\boldsymbol{\epsilon}}^v$, is described according to the solidification theory (Bažant and Prasannan, 1989a,b), and it can be formulated as

$$\dot{\boldsymbol{\epsilon}}^v(t) = \frac{1}{v(\alpha)}\dot{\boldsymbol{\gamma}}; \quad \boldsymbol{\gamma} = \int_0^t \Phi(t_r(t) - t_r(\tau))\mathbf{G}\dot{\boldsymbol{\sigma}}\mathrm{d}\tau \tag{4}$$

where $\dot{\boldsymbol{\gamma}}$ is the visco-elastic micro-strain rate of cement gel. The aging function, $v(\alpha)$, represents the volume fraction of cement gel produced by early-age chemical reactions and it depends on the total reaction degree, α, which will be discussed later in this paper.

The non-aging micro-compliance function of cement gel is defined as $\Phi(t-t_0) = q_2 \ln\left[1 + (t-t_0)^{0.1}\right]$, in which $t - t_0$ is the loading time duration, q_2 (in MPa^{-1}), is a model parameter. It is worth noting that although the viscoelastic strain of the cement gel, $\boldsymbol{\gamma}(t)$, is fully recoverable upon unloading, the macroscopic viscoelastic strain, $\boldsymbol{\epsilon}^v$, is only partially recoverable due to the effect of aging traduced by the function $v(\alpha)$.

Function $t_r(t)$ in Eq. (4) is the so-called reduced time and it represents the direct effect of temperature and relative humidity on the nano-scale creep mechanisms. According to Bažant et al. (2004), one can write $t_r(t) = \int_0^t \psi(\tau)\mathrm{d}\tau$, $\psi(t) = [0.1 + 0.9h^2]\exp[Q_v/(RT_0 - RT)]$, where T = absolute temperature; T_0 = 296 K; h = relative humidity; R = gas constant; and Q_v = activation energy for the creep processes. For typical concrete mixes $Q_v/R \approx 5000$ K (Bažant et al., 2004).

The purely viscous strain rate, $\dot{\boldsymbol{\epsilon}}^f$, represents the completely irrecoverable part of the creep strain, which it has been explained in the literature by slippage between adsorbed water layers hindered in cement nanopores. Such phenomenon is believed to be affected by breakage and restoration of transverse chemical bonds promoted by changes in nanopore disjoining pressure. In addition, relaxation of stresses in the transverse bonds lead to a reduction of creep and is considered to be the reason for observed long-term aging of concrete.

Based on this interpretation, Bažant and coworkers (Bažant et al., 1997a,b, 2004) modeled purely viscous creep by introducing the concept of micro-prestress, S, which was assumed to represent an average measure of the stresses acting on the transverse nanopore bonds. Accordingly, under general temperature and relative humidity variations, viscous creep flow and evolution of microprestress can be formulated as

$$\dot{\boldsymbol{\epsilon}}^f = q_4\kappa_0 S\psi\mathbf{G}\boldsymbol{\sigma} \quad \text{and} \quad \dot{S} + \omega\kappa_0 S^2 = \kappa_1\left|\dot{T}\ln h + T\dot{h}/h\right| \tag{5}$$

where ψ is the reduced time coefficient introduced earlier, $\omega = [0.1 + 0.9h^2]\exp[Q_s/(RT_0 - RT)]$, $Q_s/R \approx 3000$ K. Finally, κ_0 (in $\mathrm{MPa}^{-1}\,\mathrm{day}^{-1}$), κ_1 (in $\mathrm{MPa\,K}^{-1}$), and q_4 (in MPa^{-1}) are material parameters that need to be calibrated from experimental data. Note that while the general formulation depends separately on κ_0, κ_1, and q_4, only parameter q_4 governs long-term basic creep behavior (Bažant et al., 2004).

2.1.2. Microplane model for cracking and damage

Cracking and damage strain, $\boldsymbol{\epsilon}^d$, is described through a modified version of the microplane model M4 (Di Luzio, 2007). In order to amalgamate the microplane theory with the formulation presented earlier it is convenient to rewrite Eq. (2) as

$$\dot{\boldsymbol{\epsilon}} = \dot{\boldsymbol{\epsilon}}^i + \dot{\boldsymbol{\epsilon}}^v + \dot{\boldsymbol{\epsilon}}^f + \dot{\boldsymbol{\epsilon}}^m - \dot{\boldsymbol{\epsilon}}^e + \dot{\boldsymbol{\epsilon}}^s + \dot{\boldsymbol{\epsilon}}^t \tag{6}$$

where $\dot{\boldsymbol{\epsilon}}^e = \overline{E}^{-1}\mathbf{G}\dot{\boldsymbol{\sigma}}$ is an average elastic strain rate that needs to be subtracted from the strain rate calculated according to the microplane model in order to extract the cracking/damage strain: $\dot{\boldsymbol{\epsilon}}^d = \dot{\boldsymbol{\epsilon}}^m - \dot{\boldsymbol{\epsilon}}^e$. Parameter $\overline{E}$, according to the original microplane formulation, has the meaning of average elastic modulus and serves as dimensional parameter for the microplane boundaries (see Appendix A). On the contrary, in the current formulation $\overline{E}$ does not have physical meaning, since it is introduced only for numerical convenience, and it can be assigned to be (prior to the model calibration and without loss of generality) the estimated concrete elastic modulus at 28 days using the ACI formula: $\overline{E} = 4734\sqrt{f_c'}$ where f_c' is concrete compressive strength.

According to the kinematically constrained microplane model formulation, the strain vector on each microplane is the projection of the macroscopic strain tensor. By using the matrix notation introduced in Cusatis et al. (2008) one can write:

$$\boldsymbol{\epsilon}_{\mathcal{P}} = \boldsymbol{\mathcal{P}}\boldsymbol{\epsilon}^m \tag{7}$$

where $\boldsymbol{\epsilon}_{\mathcal{P}} = [\epsilon_N\ \epsilon_M\ \epsilon_L]^{\mathrm{T}}$ is the microplane strain vector, with ϵ_N = normal strain component, ϵ_M and ϵ_L = shear strain components, and

$$\boldsymbol{\mathcal{P}} = \begin{bmatrix} N_{11} & N_{22} & N_{33} & \sqrt{2}N_{23} & \sqrt{2}N_{13} & \sqrt{2}N_{12} \\ M_{11} & M_{22} & M_{33} & \sqrt{2}M_{23} & \sqrt{2}M_{13} & \sqrt{2}M_{12} \\ L_{11} & L_{22} & L_{33} & \sqrt{2}L_{23} & \sqrt{2}L_{13} & \sqrt{2}L_{12} \end{bmatrix} \tag{8}$$

Matrix $\boldsymbol{\mathcal{P}}$ collects the components of the tensors $N_{ij} = n_i n_j$, $M_{ij} = (m_i n_j + m_j n_i)/2$ and $L_{ij} = (l_i n_j + l_j n_i)/2$; where n_i, m_i, and l_i are unit vectors defining a local cartesian coordinate system on a generic microplane. The vector n_i is orthogonal to the microplane. If the microplane orientation is defined in a global spherical coordinate system characterized by the spherical angles ϑ and φ, then one can write: $n_1 = \sin\vartheta\cos\varphi$, $n_2 = \sin\vartheta\sin\varphi$, $n_3 = \cos\vartheta$; $m_1 = \cos\vartheta\cos\varphi$, $m_2 = \cos\vartheta\sin\varphi$, $m_3 = -\sin\vartheta$; and $l_1 = -\sin\varphi$, $l_2 = \cos\varphi$, and $l_3 = 0$.

When appropriate microplane level constitutive equations are formulated, then the microplane stress vector, $\boldsymbol{\sigma}_{\mathcal{P}} = [\sigma_N\ \sigma_M\ \sigma_L]^{\mathrm{T}}$, can be calculated and the macroscopic stress tensor can be computed from the principle of virtual work:

$$\boldsymbol{\sigma} = \sigma_V\mathbf{I} + \frac{3}{2\pi}\int_\Omega \boldsymbol{\mathcal{D}}^{\mathrm{T}}(\boldsymbol{\sigma}_{\mathcal{P}} - \sigma_V\mathbf{I}_{\mathcal{P}})\mathrm{d}\Omega \tag{9}$$

where Ω is the surface of a unit hemisphere; $\sigma_V = \sigma_{ii}/3$ is the volumetric stress; $\mathbf{I} = [1\ 1\ 1\ 0\ 0\ 0]^{\mathrm{T}}$; $\mathbf{I}_{\mathcal{P}} = [1\ 0\ 0]^{\mathrm{T}}$; $\boldsymbol{\mathcal{D}} = \boldsymbol{\mathcal{P}} - \boldsymbol{\mathcal{V}}$; $\mathcal{V}_{11} = \mathcal{V}_{12} = \mathcal{V}_{13} = 1/3$ and $\mathcal{V}_{ij} = 0$ otherwise. The interested reader can find additional details of the adopted microplane constitutive

equations in Appendix A and in Bažant et al. (2000), Di Luzio (2007, 2009), and Di Luzio et al. (2010b).

Since $\boldsymbol{\sigma}_{\mathcal{P}} = \mathbf{F}_{\mathcal{P}}(\varepsilon_{\mathcal{P}}) = \mathbf{F}_{\mathcal{P}}(\mathcal{P}\boldsymbol{\epsilon}^m)$, the macroscopic stress tensor can be expressed formally as $\boldsymbol{\sigma} = \mathbf{F}(\boldsymbol{\epsilon}^m)$ and, consequently, one can write

$$\dot{\boldsymbol{\epsilon}}^m = \left(\frac{\partial \mathbf{F}}{\partial \boldsymbol{\epsilon}^m}\right)^{-1} \dot{\boldsymbol{\sigma}} \tag{10}$$

However, it must be observed that, in general, the gradient of $\mathbf{F}$ cannot be computed analytically and $\dot{\boldsymbol{\epsilon}}^m$ must be computed numerically as it will be discussed in Section 3.

2.1.3. Hygral and thermal deformations

Humidity changes cause free hygrometric strain $\boldsymbol{\epsilon}^s$ (swelling or shrinkage, for positive or negative relative humidity change, respectively) associated with changes in capillary tension, surface tension, and disjoining pressure. One can write $\dot{\boldsymbol{\epsilon}}^s = k_{sh}\dot{h}\mathbf{I}$ where the coefficient k_{sh} is assumed to be approximately constant although in the literature (Wittmann, 1982) there is evidence on its dependence on relative humidity. Such an approximation is motivated by the lack of an established formulation for such a dependence. This model for the shrinkage does not consider explicitly some real physical aspect of this deformation, i.e. changes of capillary pressures or disjoining pressure or surface tension (RILEM Committee TC-69, 1988). Consequently, some problems could arise when one takes into account hysteresis of sorption isotherms. However, the numerical simulations (see Section 6) seem to be reasonably in agreement with the experimental data. It must be mentioned here that in the literature more sophisticated model for autogenous and drying shrinkage can be found (Gawin et al., 2006b) but they are outside the scope of this paper.

Similarly, temperature changes cause thermal strain rates, which can be expressed as $\dot{\boldsymbol{\epsilon}}^t = k_t\dot{T}\mathbf{I}$ where again, the coefficient k_t is assumed to be a constant. This is approximately true at moderate temperatures although minor variations have been observed as function of temperature, relative humidity, and aging (Neville, 1997).

2.2. Heat transfer and moisture diffusion

The behavior of concrete, especially at early age, depends heavily on internal relative humidity, h, and temperature, T, whose distributions can be computed by imposing moisture mass balance and enthalpy balance equations in the volume of interest. For concrete mixes in which the binder is a combination of Portland cement and silica fume and for temperature not exceeding 90 °C, one can write (Di Luzio and Cusatis, 2009a)

$$\nabla \cdot (D_h \nabla h) - \frac{\partial w_e}{\partial h}\frac{\partial h}{\partial t} - \frac{\partial w_e}{\partial \alpha_c}\dot{\alpha}_c - \frac{\partial w_e}{\partial \alpha_s}\dot{\alpha}_s - \dot{w}_n = 0 \tag{11}$$

and

$$\nabla \cdot (\lambda_t \nabla T) - \rho c_t \frac{\partial T}{\partial t} + \dot{\alpha}_c c \widetilde{Q}_c^{\infty} + \dot{\alpha}_s s \widetilde{Q}_s^{\infty} = 0 \tag{12}$$

where D_h is moisture permeability (see Appendix B), w_e is evaporable water – adsorption/desorption isotherm (see Appendix B); α_c = hydration degree; α_s = silica-fume reaction degree; $\dot{w}_n = 0.253\dot{\alpha}_c c$ is rate of non-evaporable water; ρ = mass density of concrete; c_t = isobaric heat capacity (specific heat); λ_t = heat conductivity; c = cement content; s = silica-fume content; $\widetilde{Q}_c^{\infty}$ = hydration enthalpy; $\widetilde{Q}_s^{\infty}$ = latent heat of silica-fume reaction per unit mass of reacted silica-fume. In Appendix B one can find additional details of the formulation and Di Luzio and Cusatis (2009b) report detailed calibration and validation of the theory. It must be noted here that this theory does not account, as first approximation, for typically observed hysteresis during adsorption/desorption cycles (Feldman, 1968; Baroghel-Bouny et al., 1999), which has been recently explained by Bazant and Bazant (2012a,b) to be the consequence of two related mechanisms: snap-through instabilities during the filling or emptying of non-uniform nanopores or nanoscale asperities and the molecular coalescence, or capillary condensation, within a partially filled surface.

2.3. Cement hydration and silica-fume reaction

For the concrete mixes of interest in this study, two main early-age reactions can be identified: cement hydration – the reaction of free-water with unhydrated cement particles – and silica-fume reaction – the reaction of silica particles with portlandite. Both reactions generate calcium–silicate–hydrates (C–S–H) which is the main constituent providing stiffness and strength.

Cement hydration can be characterized by the hydration degree (Ulm and Coussy, 1995; Cervera et al., 1999a; Gawin et al., 2006a; Di Luzio and Cusatis, 2009a), α_c, that represents the fraction of Portland clinker fully reacted with water. Its evolution law can be formulated as

$$\dot{\alpha}_c = \frac{A_{c1} e^{-\eta_c \alpha_c/\alpha_c^{\infty}} e^{-E_{ac}/RT}}{1 + (a - ah)^4}\left(\frac{A_{c2}}{\alpha_c^{\infty}} + \alpha_c\right)\left(\alpha_c^{\infty} - \alpha_c\right) \tag{13}$$

where $a = 5.5$ (Di Luzio and Cusatis, 2009b); E_{ac} is the hydration activation energy; R is the universal gas constant; η_c, A_{c1}, A_{c2} are material parameters; and α_c^{∞} is the asymptotic value of the hydration reaction degree.

Similarly, the silica-fume reaction can be described through the ratio between the amount of reacted silica-fume and the total amount of silica-fume (Di Luzio and Cusatis, 2009a). The evolution of this quantity, denominated silica-fume reaction degree, α_s, can be effectively expressed as

$$\dot{\alpha}_s = A_{s1}\left(\frac{A_{s2}}{\alpha_s^{\infty}} + \alpha_s\right)\left(\alpha_s^{\infty} - \alpha_s\right) e^{-\eta_s \alpha_s/\alpha_s^{\infty}} e^{-E_{as}/RT} \tag{14}$$

where E_{as} is the activation energy of the silica-fume reaction; A_{s1}, A_{s2} and η_s are material parameters; and α_s^{∞} is the asymptotic value of silica-fume reaction degree.

Following Di Luzio and Cusatis (2009a), one can estimate the asymptotic degrees of cement hydration and silica-fume reaction as $\alpha_c^{\infty} = (1.032w/c - 0.279s/c\alpha_s^{\infty})/(0.194 + w/c)$ and $\alpha_s^{\infty} = SF^{eff}\min[1, \min(0.16, 0.4w/c)/(s/c)]$, in which SF^{eff} is the"efficiency" of silica-fume, i.e. the mass ratio between SiO_2 mass content and total mass of silica-fume; w/c is water to cement ratio; and s/c is silica-fume to cement ratio. The aforementioned material parameters can be calibrated by analyzing experimental data relevant to cement hydration and silica-fume reaction, such as, for example, temperature evolution during adiabatic tests as described in details by Di Luzio and Cusatis (2009b).

It is also useful to introduce an overall degree of reaction, α, that represents an average measure of the total binder reacted (or, equivalently, a measure of the C–S–H produced). Following de Schutter and Taerwe (1995), this can be defined as the ratio between the heat released at the given time, $Q_r(t)$, and the heat developed at the completion of all chemical reactions, Q_r^{∞}

$$\alpha(t) = \frac{Q_r(t)}{Q_r^{\infty}} = \frac{\alpha_c(t) c \widetilde{Q}_c^{\infty} + \alpha_s(t) s \widetilde{Q}_s^{\infty}}{c\widetilde{Q}_c^{\infty} + s\widetilde{Q}_s^{\infty}} \tag{15}$$

2.4. Aging model

The phenomenon known as "aging" represents the change of the macroscopic behavior of concrete directly related to the modification of the internal material structure, which, in turn, is due to

the evolution of nano- and micro-scale physical mechanisms and chemical reactions. The main macroscopic observations relevant to aging are the following:

1. Stiffness increases whereas creep decreases with age. This is partly related to the increase of solidified material as a result of cement hydration and other chemical reactions, such as silica-fume reaction. This type of aging – although continues for a long period of time – is predominant only in the first year or so of concrete life. However, reduction of creep is observed even for concretes much older than 1 year. This long-term aging was explained by physical modification in the nano-structures of C–S–H and, more specifically, by the relaxation of nano-scale self-equilibrated stress states developed during the hardening phase (Bažant et al., 2004).
2. Concrete strength, in both tension and compression, increases with age as a direct consequence of the produced C–S–H (Neville, 1997). Tensile and compressive strengths grow almost proportionally with the exception of the first few days (usually less than 3 days), during which the compressive-to-tensile strength ratio is lower than the final one (Oluokun, 1991; Oluokun et al., 1991; Kim et al., 2002, 2004). Evolution of strength with time is highly nonlinear and the strength build-up is much more significant at early-age even though it continues for several years. Experimental data show that, in most cases, up to roughly 90% of strength is typically gained in the first month after casting (Neville, 1997).
3. Concrete fracture energy also increases with age. However, the increase is not proportional to the increase in stiffness and strength and, thus, it leads to a reduction of the material characteristic length – which is proportional to stiffness and fracture energy and inversely proportional to the square of tensile strength (Hillerborg, 1985). This is mainly due to an intrinsic embrittlement of C–S–H and to the fact that fracture processes in concrete are not only dependent on the properties of cement gel but are significantly affected by the interaction between cement gel matrix and inclusions (aggregate particles as well as possible fiber reinforcing) (di Prisco et al., 2007). The reduction of material characteristic length is responsible for a more brittle behavior of old concretes, which are characterized by a steeper post-peak slope of typical load–displacement responses and a consequent faster loss of loading carrying capacity during failure (Petersson, 1980; Kim et al., 2004). See, for example, Table 2 which reports compressive strength, tensile strength, Young's modules, fracture energy, and the associated characteristic length for the experimental data of Kim et al. (2004).
4. Age also affects volume, size, and inter-connectivity of pores at different length scales. Generally speaking, old concretes tend to be denser and dryer materials than their early-age counterpart. This, in turn, changes the material properties and concrete behavior relevant to moisture diffusion and heat transfer.

In this study, the effect short-term aging on both mechanical and hygro–thermal behavior is modeled in a unified manner through the concept of overall degree of reaction introduced in the previous section (Eq. (15)). For the aging formulation relevant to the hygro–thermal problem, the reader is directed to Di Luzio and Cusatis (2009a,b).

2.4.1. Stiffness and creep

Age effect on stiffness and creep is modeled by the solidification theory (Bažant and Prasannan, 1989a), which simulates directly the growth of solidified material at early age and it does so through the so-called aging law previously introduced (see Eq. (4)). In the original formulation such aging law was expressed as function of the equivalent time (Bažant et al., 2004), whose definition, however, is difficult to extend to include the effect of multiple chemical reactions. This limitation is not shared by the degree of reaction, α, and for this reason the following aging law is proposed here

$$\frac{1}{v(\alpha)} = \left[\frac{\alpha_\infty}{\alpha}\right]^{n_\alpha} \tag{16}$$

where n_α is a material parameter that can be calibrated by simulating experimental data on aging creep.

2.4.2. Strength and fracture energy

The degree of reaction is also the main internal variable used in this study to simulate the increase of strength and fracture energy at early age. However, there are experimental evidences showing that the evolution of these properties depend not only on the degree to which the chemical reactions are completed, but also on the kinetics of these reactions. For instance, it was shown experimentally that the lower the curing temperature the higher the strength for a given degree of hydration (Verbeck and Helmuth, 1968). See also, among others, Carino (1981), Kjellsen and Detwiler (1998), and Kim et al. (1998).

On the basis of these evidences, strength evolution can be assumed to depend on the so-called aging degree, λ, defined as (Cervera et al., 1999a)

$$\dot{\lambda} = \left(\frac{T_{max} - T}{T_{max} - T_{ref}}\right)^{n_\lambda} (B_\lambda - 2A_\lambda \alpha)\dot{\alpha} \tag{17}$$

for $\alpha > \alpha_0$ and $\dot{\lambda} = 0$ otherwise. The parameter α_0 defines the value of the reaction degree at the end of the setting phase, that is when concrete may begin to be considered a solid. Values of $\alpha_0 = 0.1$—0.4 have been proposed in the literature, depending on type of cement and water-to-cement ratio (de Schutter and Taerwe, 1996). T_{max} represents the maximum temperature at which hardening of concrete is possible under standard conditions ($\approx$100 °C). T_{ref} is the reference temperature for the experimental calibration of the aging model, thus for $T = T_{ref}$, it must result $\lambda = 0$ for $\alpha \leqslant \alpha_0$ and $\lambda = 1$ for $\alpha = \alpha_\infty$. By imposing these conditions one obtains $B_\lambda = [1 + A_\lambda(\alpha_\infty^2 - \alpha_0^2)]/(\alpha_\infty - \alpha_0)$, in which n_λ, A_λ are model parameters that need to be identified from experimental data.

The concept of aging degree is used hereinafter to account for early age phenomena within the modified microplane model M4 formulation. This is achieved by assuming that the material parameters, k_1–k_7, governing the microplane constitutive equations (stress–strain boundaries, see Appendix A) are functions of λ.

Parameter k_1 scales all stress–strain boundaries in the radial direction; parameter k_2 governs the horizontal plateau of the shear (frictional) boundary which is activated under high shear deformation and high level of normal compression both typical of macroscopic compressive stress states under confinement. Parameters k_3 and k_4 define the volumetric stress boundary in compression, which is mainly activated under high compressive volumetric stresses. These first four parameters can be physically interpreted as parameters characterizing the behavior of C–S–H and its internal structure. If their ratio is held constant and for constant values of the other parameters (k_5–k_7 discussed later) the macroscopic stress–strain curves scales proportionally one to each other. Based on these observations it is reasonable to assume the following relations:

$$k_1/k_1^\infty = k_2/k_2^\infty = k_3/k_3^\infty = k_4/k_4^\infty = \lambda \tag{18}$$

where k_1^∞, k_2^∞, k_3^∞, are k_4^∞ are the asymptotic values of the same parameters.

Parameter k_5 governs the post-peak slopes of normal and deviatoric boundaries as well as the rate of shear behavior degradation due to tensile fracturing. This parameter modifies the slope of the softening branch of both macroscopic tension and compression

Table 1
Material parameters of the proposed constitutive law (the star symbol (*) tags an assumed value whereas the others have been calibrated on the basis of appropriate experimental data).

Parameter	Section 6.1	Section 6.2	Section 6.2b	Section 6.3	Section 6.4	Section 6.5
q_1 [MPa^{-1}]	$1.15\cdot10^{-5}$ (OPC) $1.22\cdot10^{-5}$ (HPC)	$1.2\cdot10^{-5}$	$0.5\cdot10^{-5*}$	$2.7\cdot10^{-5}$ (C-30) $1.25\cdot10^{-5}$ (C-100)	$2\cdot10^{-5}$ (NS) $1.5\cdot10^{-5}$ (HS)	$1.95\cdot10^{-5*}$
q_2 [MPa^{-1}]	$2.6\cdot10^{-5}$ (OPC) $1.4\cdot10^{-5}$ (HPC)	$3.2\cdot10^{-5}$	$3.8\cdot10^{-5*}$	$3\cdot10^{-5}$ (C-30) $2.3\cdot10^{-5}$ (C-100)	$7\cdot10^{-5}$ (NS) $4\cdot10^{-5}$ (HS)	$1.27\cdot10^{-4*}$
n_α [–]	1.2 (OPC) 1.18 (HPC)	1.9	2.6	1.6 (C-30) 0.8 (C-100)	2 (NS) 1.75 (HS)	1.5*
q_4 [MPa^{-1}]	$1\cdot10^{-6}$ (OPC) $2\cdot10^{-8}$ (HPC)	$2.7\cdot10^{-6}$	$1.2\cdot10^{-6*}$	$1.8\cdot10^{-6*}$	$1.2\cdot10^{-6*}$	$0.8\cdot10^{-6*}$
κ_0 [(MPa^2 days)$^{-1}$]	$1\cdot10^{-2*}$	$1.9\cdot10^{-3}$	$1\cdot10^{-2*}$	$2\cdot10^{-2*}$	$2\cdot10^{-2*}$	$3\cdot10^{-2*}$
κ_1 [MPa/K]	5*	20*	5.0*	5.5*	5*	5*
α_0 [–]	0.24(OPC) 0.28 (HPC)	0.24*	0.24*	0.15 (C-30) 0.1 (C-100)	0.35 (NS) 0.25 (HS)	0.2*
A_λ [–]	3.4 (OPC) 4.2 (HPC)	2.7*	0.6*	0.5 (C-30) 0.2 (C-100)	4.2 (NS) 4.7 (HS)	0.05*
n_λ [–]	0.3*	0.3*	0.3*	0.8 (C-30) 0.1 (C-100)	0.3 (NS) 0.3 (HS)	0.3*
k_1^∞ [–]	$212\cdot10^{-6}$ (OPC) $342\cdot10^{-6}$ (HPC)	$215\cdot10^{-6}$	$212\cdot10^{-6}$	$148\cdot10^{-6}$ (C-30) $296\cdot10^{-6}$ (C-100)	$159\cdot10^{-6}$ (NS) $217\cdot10^{-6}$ (HS)	$208\cdot10^{-6*}$
k_2^∞ [–]	500*	500*	500*	500*	500*	500*
k_3^∞ [–]	10*	10*	10*	10*	10*	10*
k_4^∞ [–]	150*	150*	150*	150*	150*	150*
k_5^∞ [–]	0.6 (OPC)* 0.7 (HPC)*	0.57*	0.57*	1 (C-30)* 1 (C-100)*	3 (NS) 2.1 (HS)	0.6*
k_6^0 [–]	1.74 (OPC)* 2.1 (HPC)*	1.74*	1.74*	2 (C-30)* 3 (C-100)*	2 (NS) 2.8 (HS)	1.9*
k_6^∞ [–]	0.87 (OPC)* 0.7 (HPC)*	0.87*	0.87*	1 (C-30)* 0.8 (C-100)*	0.98 (NS) 0.7 (HS)	0.88*
λ_0 [–]	0.5*	0.4*	0.4*	0.5 (C-30)* 0.5 (C-100)*	0.5 (NS) 0.7 (HS)	0.4*
k_7^∞ [–]	200*	200*	200*	200	200*	200*
n_7 [–]	1.0 (OPC)* 1.1 (HPC)*	1.0*	1.0*	1.0 (C-30) 2.0 (C-100)	1.0 (NS)* 2.0 (HS)*	1.0*
k_{sh} [–]	$2.5\cdot10^{-3*}$	$1.9\cdot10^{-3}$	$9\cdot10^{-4}$	$1.2\cdot10^{-3*}$	$5\cdot10^{-4*}$	$1.6\cdot10^{-3*}$
k_t [–]	$1\cdot10^{-5*}$	$1\cdot10^{-5*}$	$1\cdot10^{-5*}$	$1\cdot10^{-5*}$	$1\cdot10^{-5*}$	$1\cdot10^{-5*}$
$\bar{E}$ [MPa]	44,000 (OPC) 53,700 (HPC)	30,820	30,820*	29,700 (C-30) 46,400 (C-100)	38,840 (NS) 31,300 (HS)	31,000*

stress–strain curves. From a physical point of view, k_5 can be interpreted as representative of mechanical interlocking and bridging effects occurring at the scale of aggregate particles. Such mechanical interaction is assumed in this study to be approximately age independent, $k_5 \approx k_5^\infty$ = constant, even though, arguably, age could have an effect on the behavior of the interface between aggregate and cement paste. As it will be shown later in this paper, this approximation does not limit the ability of the overall formulation to simulate relevant experimental data.

Parameter k_6 scales vertically the normal stress boundary and the frictional cohesion. It affects also the so called "transition function" governing the behavior of the normal stress component as far as the volumetric–deviatoric coupling is concerned (see Appendix A and Di Luzio (2007) for a detailed discussion of the transition function). Macroscopically, an increase of k_6 leads to an increase of the tensile strength without significantly affecting the compressing strength. Consequently, it can be used to control the ratio between tensile strength and compression strength. As discussed earlier, experimental evidence exists showing a decrease of such a ratio with age. This can be captured by setting

$$k_6 = \begin{cases} k_6^0 - (k_6^0 - k_6^\infty)\lambda/\lambda_0 & \text{for } 0 \leqslant \lambda \leqslant \lambda_0 \\ k_6^\infty & \text{for } \lambda_0 \leqslant \lambda \leqslant 1 \end{cases} \tag{19}$$

where k_6^0 and k_6^∞ are initial and asymptotic values, respectively, of the k_6 parameter.

Finally, parameter k_7 governs the softening branch of the deviatoric boundaries and, by keeping constant the other parameters, it modifies mainly the post-peak softening behavior under macroscopic compression: the smaller k_7 is, the steeper the macroscopic post-peak slope in compression results. This parameter can be then used to simulate embrittlement due to aging by setting $k_7/k_7^\infty = \lambda^{-n_7}$.

3. Numerical implementation

The presented theory needs to be integrated numerically and this task is achieved on the basis of a finite element framework consisting of two main components: (1) a finite element solver for the solution of the hygral–thermal problem including the integration of the evolution equations of the degree of reaction; and (2) a finite solver for the solution of the mechanical problem given the solution of the hygral–thermal problem. It must be observed that no effect of the mechanical problem to the hygro–thermal problem is considered here and consequently the two numerical solutions can be carried out in series, with the hygro–thermal problem to be solved before the mechanical one.

The numerical integration of the hygral–thermal problem was discussed in detail in Di Luzio and Cusatis (2009b) to which the reader is referred for details. The Dirichlet's boundary conditions are directly imposed on the system, whereas Cauchy's boundary conditions are enforced approximately by considering an additional layer of material attached to the actual boundaries and imposing Dirichlet's boundary conditions on these fictitious boundaries (Bažant and Najjar, 1972; Di Luzio and Cusatis,

Table 2
Evolution of the characteristic length estimated using data from Kim et al. (2004).

Concrete type	Age [days]	f_c [MPa]	f_t [MPa]	E [GPa]	G_f [N/m]	l_{ch}
LS	1	3.92	0.28	7.649	22.08	2154.21
	3	10.30	1.54	19.515	103.83	854.38
	7	13.73	1.80	21.673	106.77	714.21
	14	15.59	2.43	23.043	106.8	416.82
	28	18.53	2.90	26.772	106.81	340.01
NS	1.5	5.49	1.56	12.945	83.93	446.45
	3.5	16.48	2.23	22.948	142.38	657.03
	7.75	22.36	3.27	26.184	106.8	261.52
	14.75	26.58	3.7	26.87	104.65	205.40
	28.5	33.24	3.92	28.832	127.74	239.68
HS	1	16.57	2.9	24.32	86.44	249.97
	3.25	26.18	3.85	31.283	101.49	214.2
	7.33	37.27	3.91	32.46	138.84	294.79
	14.75	52.07	4.59	33.833	124.08	199.26
	28	57.96	4.86	35.794	119.04	180.4

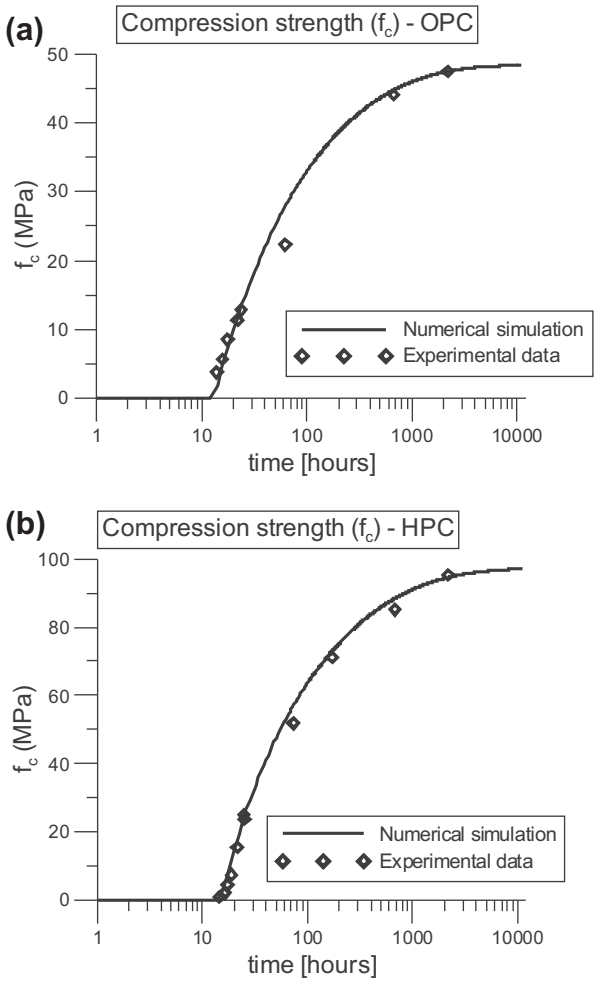

Fig. 2. Evolution of the compressive strength for (a) ordinary portland concrete (OPC) and (b) a high-performance concrete (HPC).

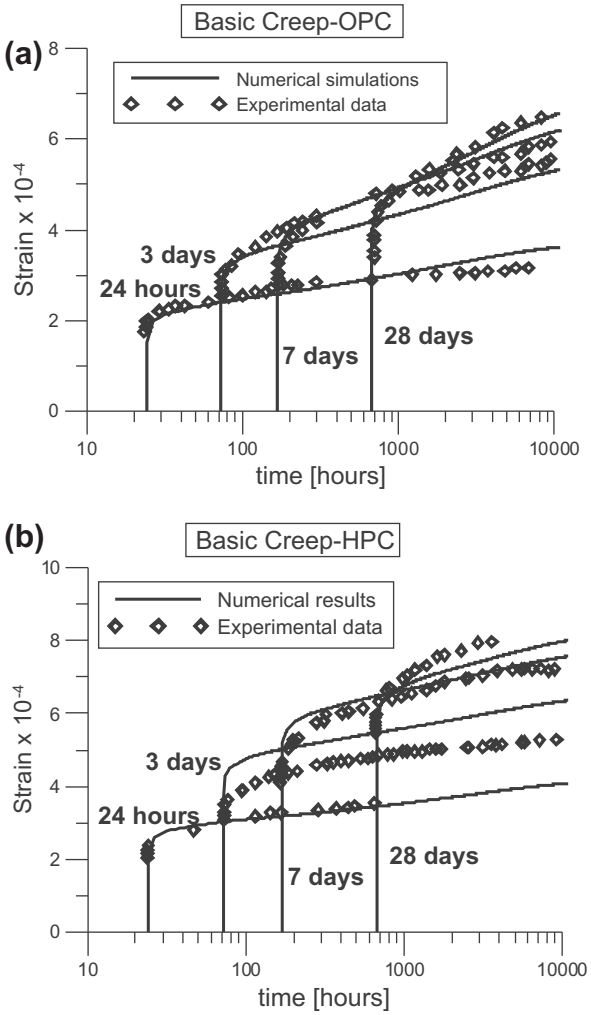

Fig. 3. Strain versus time under constant load at different ages for (a) ordinary portland concrete (OPC) and (b) a high-performance concrete (HPC).

2009b). By changing the thickness of the additional layer (usually between 1 and 5 mm), different heat and moisture surface emissivity coefficients can be simulated.

The nonlinear finite element solution of the mechanical problem is a very well established subject (see, among many others, Belytschko et al. (2000)) if the constitutive equation can be integrated in rate form; i.e. it provides, for a generic time step, $\Delta t_n = t_{n+1} - t_n$, the stress increment, $\Delta\boldsymbol{\sigma}_n$, associated to the total strain increment, $\Delta\boldsymbol{\epsilon}_n$.

For the present constitutive equation this can be achieved as follows.

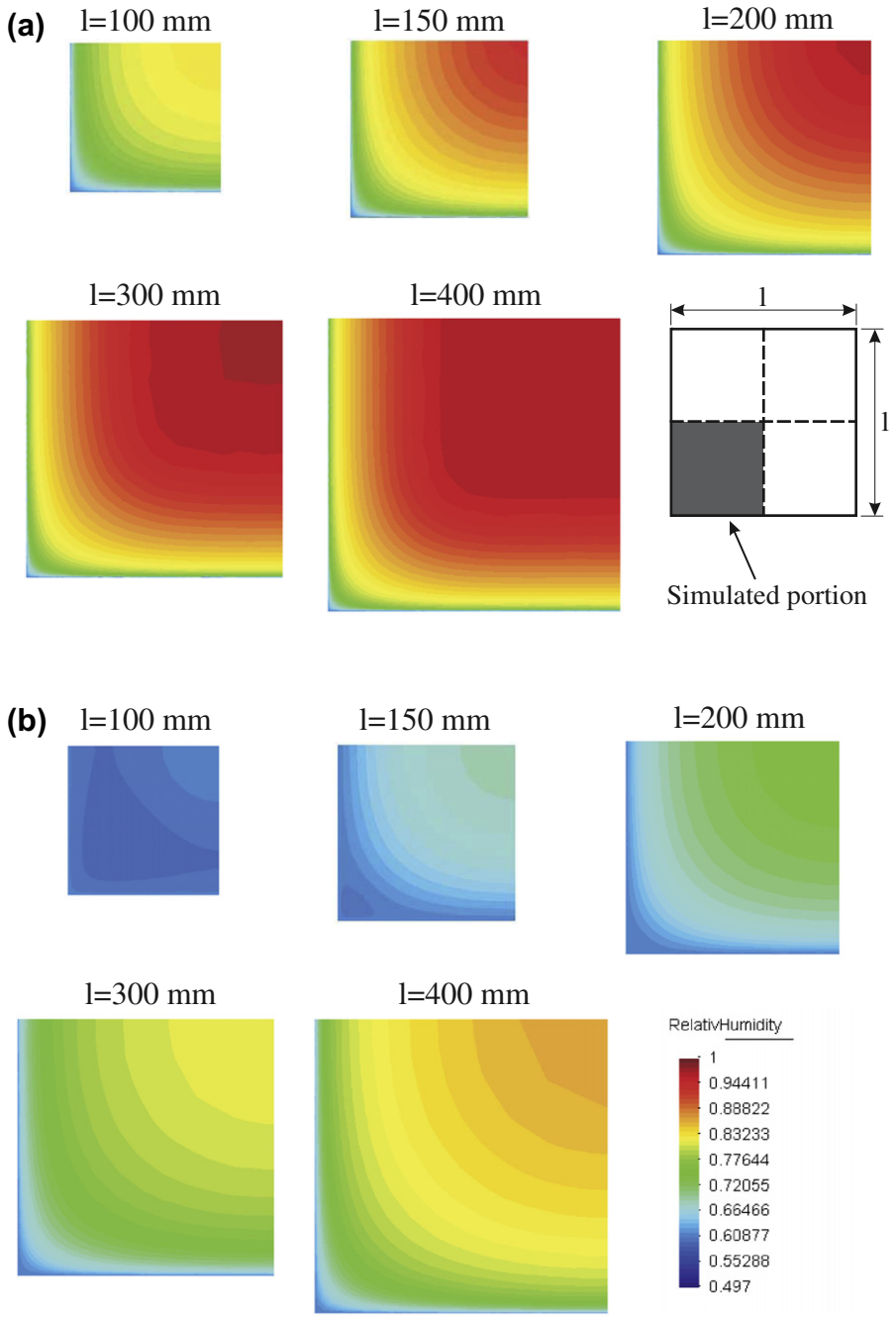

Fig. 4. Relative humidity distribution after (a) 28 days and (b) 182 days for different cross section size for the prism specimens of Bryant and Vadhanavikkit (1987) tests (figures are not drawn to scale).

By using a Kelvin chain approximation of the visco-elastic strain and the exponential algorithm (Jirásek and Bažant, 2002), the stress increment can be written as

$$\Delta\boldsymbol{\sigma}_n = \mathbf{E}_n\left(\Delta\boldsymbol{\epsilon}_n - \Delta\boldsymbol{\epsilon}''_n - \Delta\boldsymbol{\epsilon}^m_n\right) \tag{20}$$

where $\mathbf{E}_n = [C_n\mathbf{G}]^{-1}$ is the incremental visco-elastic stiffness matrix; $C_n = q_1 + C^v_n + C^f_n - \bar{E}^{-1}$ is the incremental visco-elastic compliance; $\Delta\boldsymbol{\epsilon}''_n = \Delta\boldsymbol{\epsilon}^{v''}_n + \Delta\boldsymbol{\epsilon}^{f''}_n + k_s\Delta h_n\mathbf{I} + k_t\Delta T_n\mathbf{I}$ includes the imposed strain increments due to the visco-elastic and viscous flow as well as hygro–thermal effects. For additional details on the numerical implementation of the solidification–microprestress theory the reader is referred to the additional details in Appendix C and to the detailed discussion in Bažant et al. (1997b, 2004).

In Eq. (20), the strain increment $\Delta\boldsymbol{\epsilon}^m_n$ needs to be calculated according to the microplane model and this requires an iterative algorithm within the time step because, unlike the other terms, the microplane model strain increment depends nonlinearly on the stress increment. In the following the numerical procedure proposed by Di Luzio (2009) is exploited. Accordingly, the stress increment can be rewritten as $\Delta\boldsymbol{\sigma}_n = \boldsymbol{\sigma}_{n+1} - \boldsymbol{\sigma}_n = \mathbf{F}(\boldsymbol{\epsilon}^m_n + \Delta\boldsymbol{\epsilon}^m_n) - \boldsymbol{\sigma}_n$, which introduced in Eq. (20) gives

$$\mathbf{F}\left(\boldsymbol{\epsilon}^m_n + \Delta\boldsymbol{\epsilon}^m_n\right) + \mathbf{E}_n\Delta\boldsymbol{\epsilon}^m_n = \mathbf{E}_n\left(\Delta\boldsymbol{\epsilon}_n - \Delta\boldsymbol{\epsilon}''_n\right) + \boldsymbol{\sigma}_n \tag{21}$$

Eq. (21) is a nonlinear system of equation in which the only unknown is the strain increment $\Delta\boldsymbol{\epsilon}^m_n$. This system of equations can be solved accurately and efficiently by using the algorithm

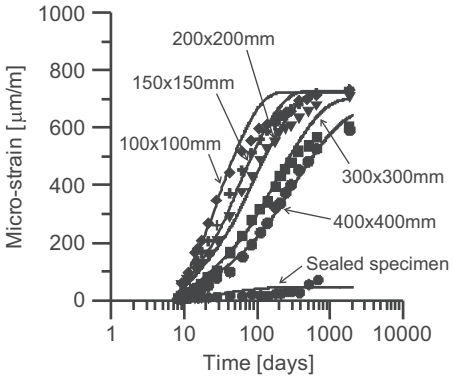

Fig. 5. Fit of shrinkage strain by Bryant and Vadhanavikkit (1987).

proposed in Di Luzio (2009) that uses a solution strategy in which the first three Newton–Raphson iterations are followed by Broyden iterations to accelerate convergence. In most cases the algorithm is very stable and it converges in less than 10 iterations.

4. Model calibration

Calibration of the chemo–thermal–hygro (CTH) model was discussed in detail by the authors in Di Luzio and Cusatis (2009b). Since experimental data to calibrate the CTH model are not always available, an educated guess is often necessary. In the current study, unless otherwise noted, the following CTH parameters were used: $\rho = 2400$ kg/m^3; $c_t = 1100$ J/kg °C; $\lambda_t = 5.4$ W/m °C; $\widetilde{Q}_c^{\infty} = 500$ kJ/kg; $\widetilde{Q}_s^{\infty} = 780$ kJ/kg; $E_{ac}/R = 5000$ K; $E_{as}/R = 9700$ K; $E_{ad}/R = 2700$ K; $SF^{eff} = 0.9$; $\kappa_c = 0.253$; $g_1 = 2.2$; $k_{vg}^c = 0.2$; $k_{vg}^s = 0.3$; $A_{c1} = 2.5 \cdot 10^7$ h^{-1}; $A_{c2} = 5 \cdot 10^{-3}$; $\eta_c = 7.5$; $A_{s1} = 50 \cdot 10^{13}$ h^{-1}; $A_{s2} = 1 \cdot 10^{-6}$; $\eta_s = 9.5$; $D_0 = 1 \cdot 10^{-4}$ [kg/mm h]; $D_1 = 2$ [kg/mm h]; $n = 4$.

The mechanical response of the solidification–microprestress–microplane (SMM) model also depends on a number of material parameters that need to be calibrated by fitting experimental data. The calibration and validation of the SMM model parameters have been already presented in a previous publication (Di Luzio and Cusatis, 2012). In the following only a brief description is reported. Basic creep parameters, q_1, q_2, q_4, and n_α, can be identified by fitting experimental data on basic creep relevant to at least two concrete ages. Calibration of parameters κ_0, and κ_1 require creep data at variable humidity and temperature. Aging microplane parameters, governing aging strength (uniaxial and multiaxial) and fracture energy, k_1^{∞}, k_2^{∞}, k_3^{∞}, k_4^{∞}, k_5^{∞}, k_6^{∞}, k_7^{∞}, k_6^0, λ_0, A_λ and n_λ, n_7, can be calibrated through fitting experimental data relevant to unconfined compressive strength, triaxial tests, and fracture tests. Finally, coefficients k_t and k_{sh} can be calibrated by fitting experimental data on thermal expansion and shrinkage, respectively. Once the model calibration is performed, model validation can be carried out by simulating experimental data, relevant to the same concrete of the calibration, that has not been used in the calibration phase. However, in the validation phase, parameter adjustment is not permitted.

In the current literature, a comprehensive study providing, for the same concrete, all experimental data needed for the calibration of the proposed model, is not available. In most of the cases, experimental investigations tend to analyze specific aspects in relation to different mixes more that focusing on a thorough analysis of one single mix. In these cases, the only option left is an educated guess of the parameters that cannot be calibrated directly. Table 1 reports the model parameters used in this study. Values identified with the star symbol (*) are assumed rather than calibrated due to the lack of relevant experimental data.

To suppress spurious mesh sensitivity and to prevent the damage from localizing into a zone of zero volume, the continuum theory must be complemented by certain conditions called 'localization limiters' (Di Luzio and Bažant, 2005). As the simplest localization limiter, one may adjust the post-peak slope of the stress–strain diagram as a function of the element size. This is done in the crack band model (Bažant and Oh, 1983) which is the model most widely used in practice. This type of localization limiters is adopted for regularizing the microplane model M4 adjusting the free parameter k_5^{∞} according to the crack band width h. For solid eight node elements the crack band width is assumed to be equal to the average element size $h = V^{1/3}$, where V is the volume of the finite element.

5. Discussion of model limitations and caveats

The computational framework presented in the previous sections has a number of appealing features which, as will be shown clearly hereinafter, allows simulating typical experimental evidences relevant to concrete behavior at various ages – from few days to several years. Nevertheless, the formulation, for the sake of simplicity and practicality, is not completely general and the lack of generality as well as specific limitations need to be evaluated carefully when considering the range of applicability of the model.

The model accounts for the effect of relative humidity and temperature on the mechanical behavior of concrete but does not consider the effect of the mechanical response on the hygro–thermal problem. This limitation does not allow simulating the increased diffusivity of concrete due to cracking and fracture leading to potentially inaccurate calculation of relative humidity

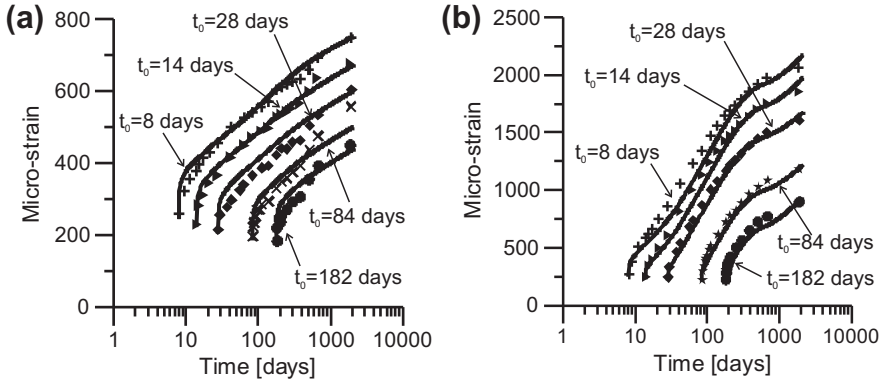

Fig. 6. Fit of basic creep (a) and total strains (b) at drying by Bryant and Vadhanavikkit (1987).

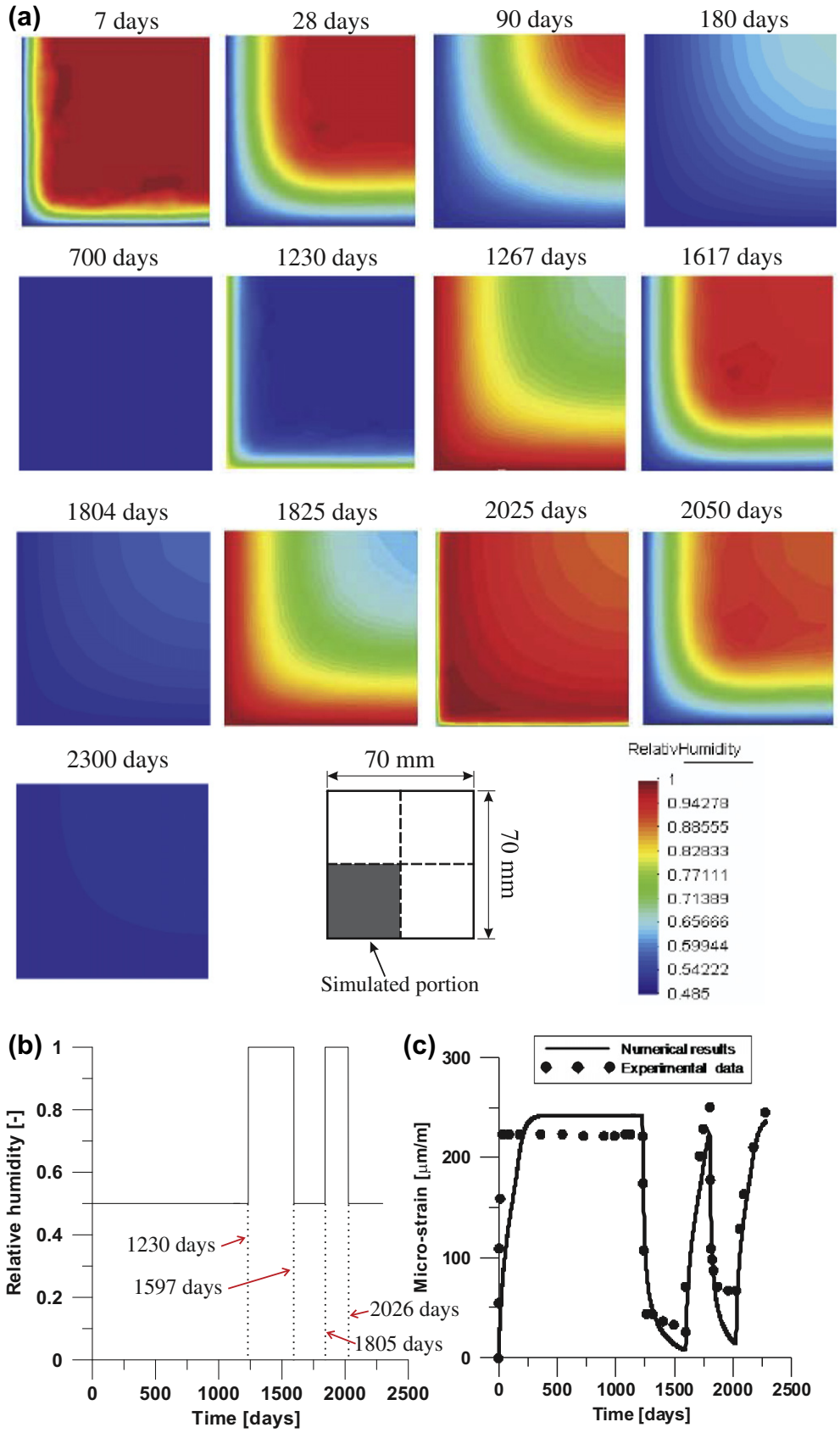

Fig. 7. Relative humidity distribution (a), its imposed external story (b), and the corresponding shrinkage strain for the prism specimens of L'Hermite et al. (1965) tests.

distributions in regions of concrete members subject to tensile stresses (e.g. members in bending).

The thermodynamic consistence of the basic microplane model formulation has been investigated by many authors in the

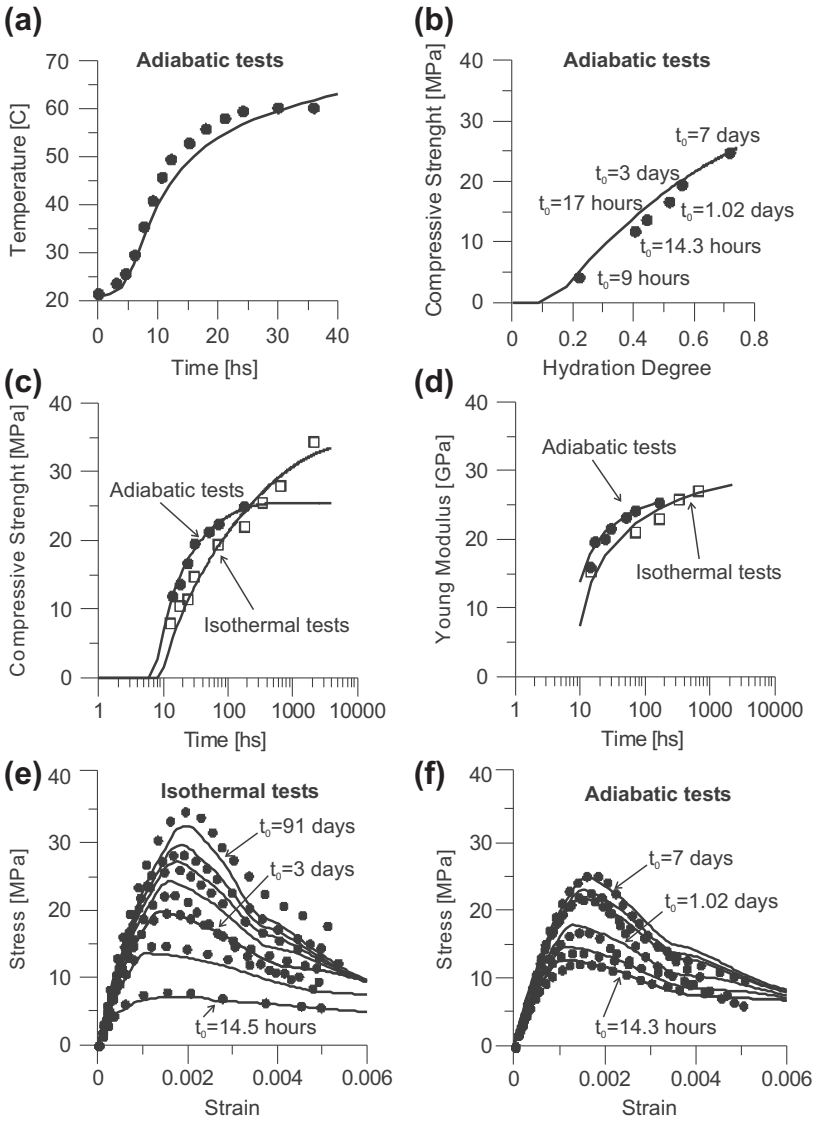

Fig. 8. Fit of experimental results for C-30 concrete (Khan et al., 1995).

literature (Carol et al., 2001) and it could not be demonstrated in general without the use of microplane potentials. However, formulations with microplane potentials have not shown the same ability of reproducing concrete behavior as other type of formulations similar to the one adopted in the M4 version used in this paper. Consequently, M4-type formulations have been favored in the literature. It must be pointed out that despite this limitation, M4-type formulations have been extremely successful in reproducing concrete behavior under a very large number of loading conditions and never thermodynamic inconsistencies were ever observed. The current formulation does inherit the same type of limitations and wide applicability. Furthermore, a comprehensive thermodynamic analysis of the overall formulation including the effect of aging as well as hygro–thermal variations is warranted in the future.

6. Numerical simulation of experimental data

6.1. Aging creep and strength build-up

The first numerical example deals with simulation of experimental data reported in Laplante (1993), in which two different concrete mixes were tested: (1) an ordinary Portland concrete (OPC) with a water-to-cement ratio, w/c, equal to 0.5; and (2) a high-performance concrete (HPC) with silica fume, $s/c = 0.1$, and $w/c = 0.3$. In this experimental campaign, cylindrical specimens of diameter 160 mm and length 100 mm were used to perform unconfined compression tests and creep tests at different ages. Temperature, relative humidity, and degree of reaction evolution and the degree of hydration is obtained by solving the hygro–thermo–chemical problem with $T = 21$ °C and sealed condition for the water at the specimen surface. Since, in these tests, the temperature and humidity fields do not feature significant spatial gradients, all the numerical simulations were carried out on a single element mesh subjected to boundary conditions corresponding to isothermal heat exchange without water mass exchange. The SMM model parameters used in the numerical simulations are reported in the first column of Table 1.

Fig. 2a (for OPC) and b (for HPC) shows comparison between experimental data and numerical simulations as far as the evolution of compressive strength is concerned. The agreement between experiments and simulations is very good; the model predicts the onset of strength build up between 10 and 11 h after casting for both OPC and HPC and the asymptotic strength to be 9% and

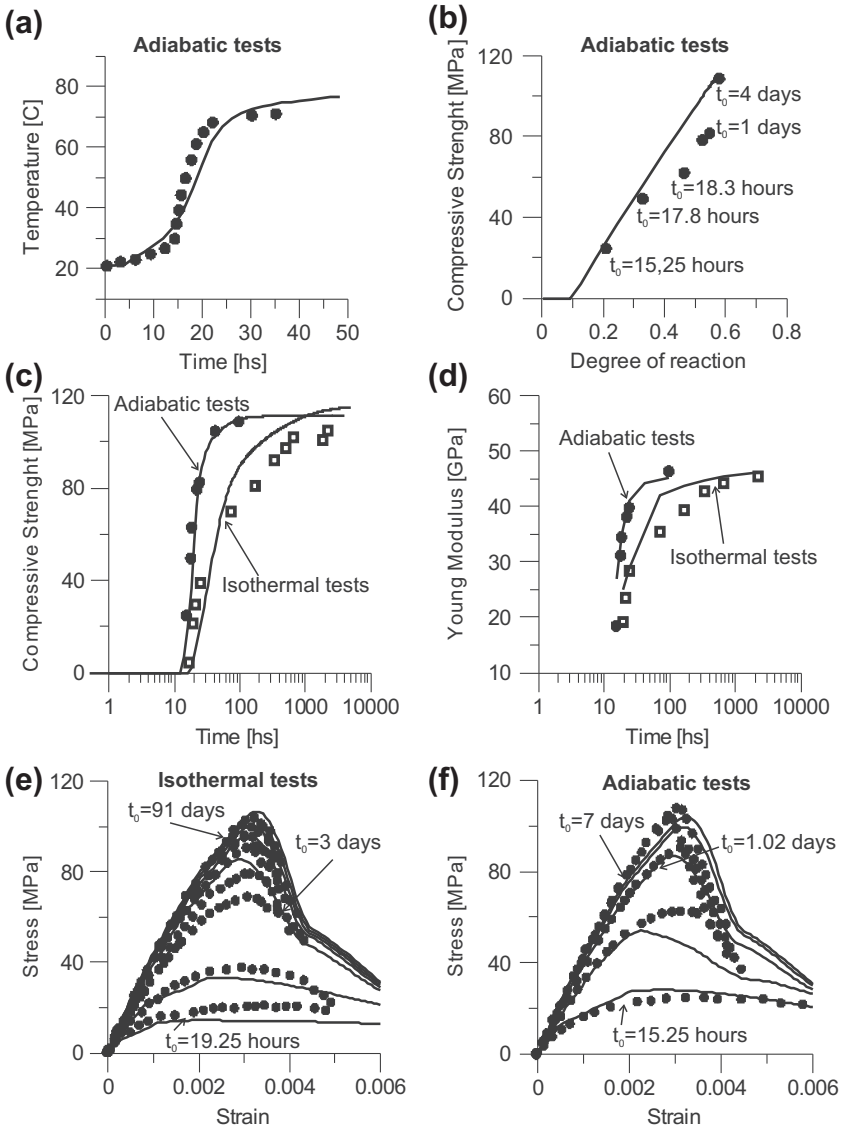

Fig. 9. Fit of experimental results for C-100 concrete (Khan et al., 1995).

12.2% higher than the 28 days strength, 44.08 MPa for OPC and 85.13 MPa for HPC, respectively.

Fig. 3a and b shows results relevant to creep tests in terms of strain versus time curves for OPC and HPC, respectively, loaded at t = 1, 3, 7, and 28 days. It must be noted here that the creep tests were carried out by applying unconfined compressive stresses of 30% of the compressive strength at the age of loading; consequently the strain curves in Fig. 3a and b are actually relevant to different level of stress (3.92, 7.65, 10.26, and 13 MPa for OPC; 7.46, 15.54, 21, and 25.5 MPa for HPC). The corresponding creep functions (strain per unit stress) are reported in Fig. 3c and d and they show that the model is able to predict well aging effect on concrete creep.

6.2. Shrinkage and drying creep

The experimental investigation of Bryant and Vadhanavikkit (1987) is considered in this section. Bryant and Vadhanavikkit (1987) used 600 mm long prims with square cross section of various sizes (from 150 mm to 400 mm) to measure shrinkage strains under both sealed conditions and drying with environmental relative humidity of 60% and temperature of 20 °C. In addition, they performed basic and drying creep tests by applying a 7 MPa compressive stress under the same aforementioned environmental conditions. Creep tests were conducted only on the 150 × 150 × 600 mm prismatic specimens.

A concrete mix with the following characteristics was used: ordinary Portland cement (390 kg/m^3) with $w/c = 0.47$; without additives; with crushed basalt aggregates (1667 kg/m^3 and maximum size of 24 mm) and silica sand (318 kg/m^3). All the specimens were cured for 8 days in a controlled environment room at 20 °C and 95% relative humidity, after that, they were exposed to drying at the aforementioned environmental conditions and then tested at different ages.

Moisture distribution and degree of hydration were calculated by solving the hygro–thermo–chemical model with the standard parameters reported earlier in this paper and $D_0 = 0.00002$ [kg/mm h]; $D_1 = 2.5$ [kg/mm h]; $n = 6.5$. The used parameters for the mechanical model are shown in the second column of Table 1 and the results of the relative humidity distribution are summarized in Fig. 4.

As one can see, the model captures well the shrinkage size-effect, that is larger specimens are characterized by a smaller shrinkage rate although the asymptotic shrinkage is the same. This is

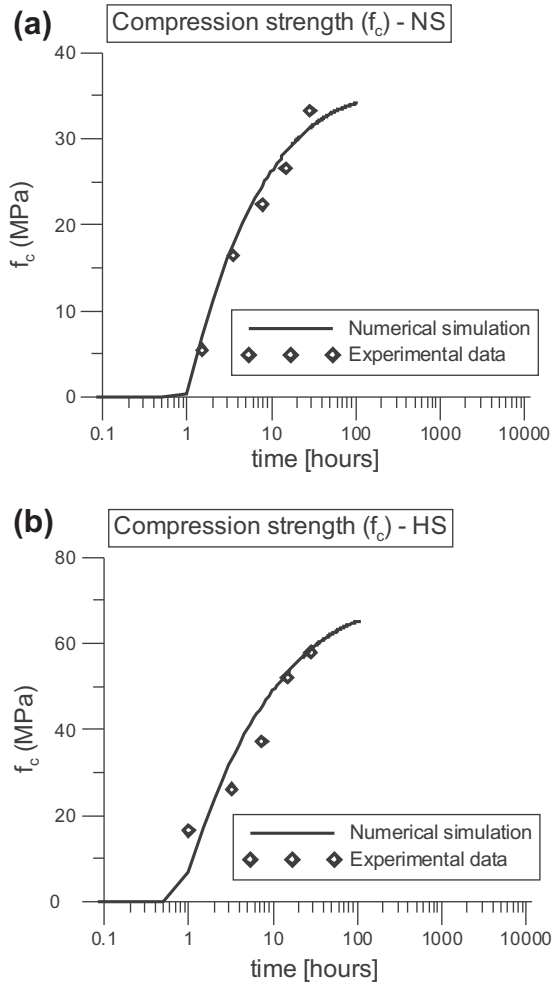

Fig. 10. Evolution of the compressive strength for (a) normal strength concrete (NC) and (b) high strength concrete (SC).

obviously due by the moisture diffusion process that is slower in larger specimens than in small ones. Fig. 5 shows the relative humidity distribution at $t = 28$ and $t = 182$ days for cross section size of 100, 200, and 400 mm, in which only 1/4 of the cross section has been modeled using the proper symmetric conditions. One can see that after 182 days, the center of the 100 mm specimen have already started to dry while the one of the 400 mm is still at high relative humidity condition.

In addition, Fig. 6 shows the best fits achieved for the basic creep (Fig. 6a) and for drying creep (Fig. 6b) with different ages of loading, namely $t_0 = 8,\ 14,\ 28,\ 84$, and 182 days. It is worth noting here that the reported strains are total strains, i.e. they include creep strain due to loading; shrinkage strain due to drying and self desiccation; and cracking strain developed prior to load application. As one can see, the numerical results are in very good agreement with the experiments for both basic and drying creep.

A second experimental investigation of L'Hermite et al. (1965) is also considered in this section. L'Hermite et al. (1965) used square prisms with length of 280 mm base size of 70 mm to measure shrinkage strain under drying with variable relative humidity.

A concrete mix with the following characteristics was used: ordinary Portland cement (350 kg/m^3) with $w/c = 0.45$; without additives; with 1900 kg/m^3 of aggregates.

Moisture distribution and degree of hydration were simulated by solving the hygro–thermo–chemical model with the standard parameters reported earlier in this paper and $D_0 = 0.0003$ [kg/mm h]; $D_1 = 0.1$ [kg/mm h]; $n = 6.0$. The used parameters for the mechanical model are shown in the third column of Table 1. Fig. 7a shows the relative humidity distribution and evolution until $t = 2300$ days for the external story of relative humidity condition reported in Fig. 7b. One can see that the small cross section allows the center of the specimen to dry quite soon (less than 1 year). As it can be seen from Fig. 7c, the model captures relatively well the shrinkage evolution, confirming that the simple model for shrinkage adopted in the present formulation simulated quite well drying shrinkage.

6.3. Short-term mechanical properties

In the third numerical example, the experimental tests carried out by Khan et al. (1995) are considered. Two different mixes were studied: an ordinary Portland concrete, referred as C-30, and a high-strength concrete, referred as C-100 (30 and 100 MPa being approximately the 28-day concrete strengths, respectively).

C-30 contained Portland cement (355 kg/m^3) with $w/c = 0.5$, fine aggregate (790 kg/m^3), coarse aggregate (1040 kg/m^3), and no superplasticizer. C-100 used a type 10 blended cement (540 kg/m^3) containing 9% silica fume (42.3 kg/m^3) with water-to-binder ratio equal to 0.25, a high dose of superplasticizer (19.5 kg/m^3), fine aggregate (720 kg/m^3), and coarse aggregate (1105 kg/m^3). Additional details of the composition and properties of these concretes mixes can be found in the original experimental publication (Khan et al., 1995).

Concrete cylinders of 100 × 200 mm were used to measure the stress–strain curves relevant to concrete ages ranging from 14 h to 91 days and for different curing conditions. From these stress–strain curves concrete strength and young modulus were obtained through peak stress and initial slope, respectively.

Standard parameters for the HTC model were adopted with the exception of parameters $A_{c1} = 3 \cdot 10^7$ h^{-1} and $A_{c2} = 1 \cdot 10^{-4}$ for C-30 and $A_{c1} = 2 \cdot 10^7$ h^{-1}; $A_{c2} = 1 \cdot 10^{-4}$; $\eta_c = 3$; $A_{s1} = 5 \cdot 10^7$ h^{-1}, $A_{s2} = 1 \cdot 10^{-6}$, $\eta_s = 9.5$ for C-100 which were calibrated by fitting temperature rises under adiabatic tests. All the numerical simulations were carried out on a single element mesh subjected to boundary conditions corresponding to isothermal or adiabatic heat conditions and without water mass exchange, consistently with the experimental procedure. Used parameters for the SMM model are reported in the third column of Table 1.

Figs. 8 and 9 summarize, for C-30 and C-100, respectively, the comparison between the experimental data and the numerical results for a variety of different tests that were analyzed in this study. In these figures symbols represent the experimental values and solid lines are the results of numerical simulations.

Figs. 8a and 9a show the evolution of temperature in time during adiabatic tests. Temperature is due to the heat generated by cement hydration and silica-fume reaction. Both experiments and simulations show the maximum temperature raise between 5 and 10 h for C-30 and 15 and 20 h for C-100. For the same tests, Figs. 8b and 9b present the experimental and calculated dependence of compressive strength versus degree of reaction (hydration for C-30; hydration and silica-fume reaction for C-100).

Figs. 8c and 9c show the evolution of compressive strength whereas Figs. 8d and 9d show the evolution of Young's modulus, for C-30 and C-100, respectively. Each of this figure shows experimental points and numerical curves for two curing conditions: adiabatic and isothermal (T = 21 °C). Results show that the proposed model replicates well the experimental behavior for both concrete mixes and curing conditions. In particular, the model predicts more rapid strength and Young's modulus gains when subjected to adiabatic curing, but higher asymptotic compressive strength and Young's modules under isothermal curing than under adiabatic curing. The different behavior observed for adiabatic curing versus isothermal curing is much more pronounced for C-30 than

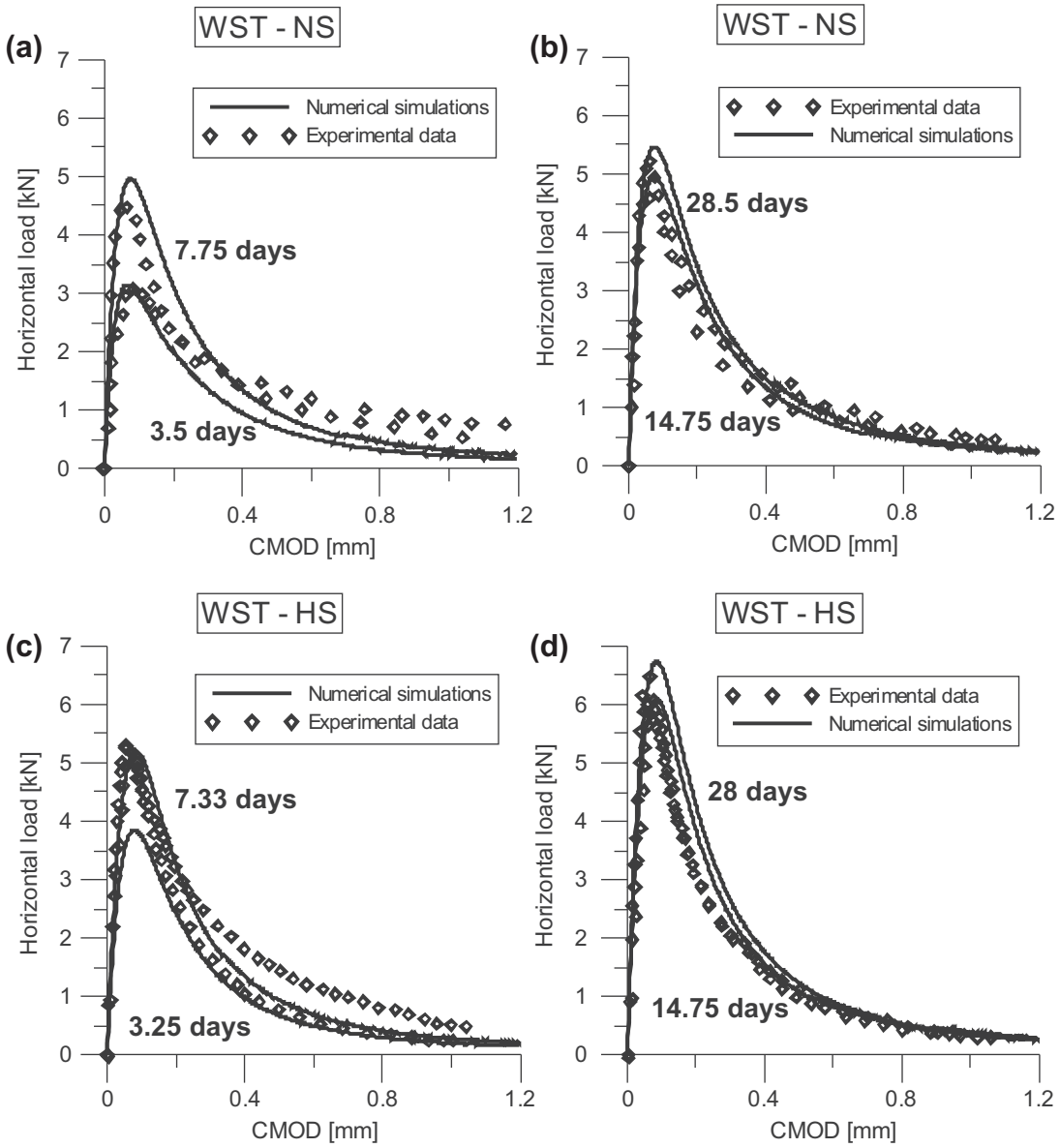

Fig. 11. Strain versus time under constant load at different ages for (a) ordinary portland concrete (OPC) and (b) a high-performance concrete (HPC).

for C-100. For example, while for C-100 the asymptotic strength under isothermal conditions is only slightly higher than the one under adiabatic conditions, for C-30 such a difference is significant (about 30%). This is due to the effect of the temperature on both the degree of reaction (Eqs. (13)–(15)) and the aging degree (Eq. (17)).

Finally, complete stress–strain curves for uniaxial compression tests carried out at different concrete ages are reported in Figs. 8e and 9e for isothermal tests and in Figs. 8f and 9f for adiabatic tests. The agreement between the computed and experimental results is remarkable, both in the prediction of the aging effect (corresponding to the evolution of the compressive strength and the elastic modulus) and in the description of the nonlinear part of the stress–strain curves (both pre-peak and post-peak). It must be stressed again here, that these results were all obtained by using the same model parameters. This shows excellent capability of the model to simulate properly influence of temperature on early age reactions (hydration and silica fume reaction) and aging phenomena.

6.4. Short-term fracturing behavior

The forth example considers the experimental investigations of Kim et al. (2004). This study investigated the fracture characteristics of concrete at early ages by using Wedge-Splitting Tests (WST) performed on notched prism specimens of width = 240 mm, height up to roller axis = 200 mm, thickness = 125 mm, and ligament = 100 mm. Two concrete mixes with type I Portland cement, super-plasticizer (high-range water-reducing admixture), and maximum aggregate size of 19 mm were used. The first mix was made of a Normal-Strength (NS) concrete with cement content = 342 kg/m^3, $w/c = 0.54$, additive content = 1.03 kg/m^3, aggregate content = 1757 kg/m^3; whereas the second mix was made of a High-Strength (HS) concrete with cement content = 533 kg/m^3, $w/c = 0.3$, additive content = 5.33 kg/m^3, and aggregate content = 1802 kg/m^3.

All the specimens were removed from the molds after 24 h and were wet-cured in a curing room with 100% relative humidity at 23 °C until the testing date. Simulating these environmental

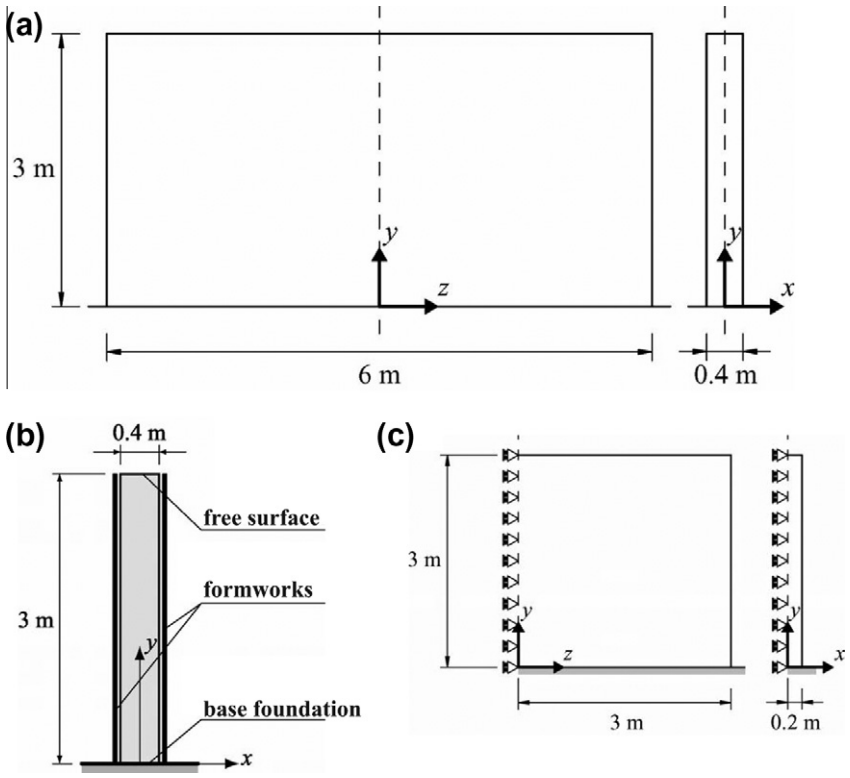

Fig. 12. Concrete wall: (a) the real geometry, (b) the geometry and the boundary condition used in the diffusion problem, and (3) the geometry and the boundary condition used in mechanical problem.

conditions, moisture distribution, temperature distribution and degree of hydration were calculated according to the HTC model with standard parameters.

Fig. 10 shows the comparison between experimental data and model simulation for the evolution of the compressive strength in time for NS and HS, respectively. Fig. 11 shows the comparison between the experimental and numerical results of the splitting load versus Crack Mouth Opening Displacement (CMOD) for NS (Fig. 11a and b) and HS (Fig. 11c and d) concretes loaded at different ages (about 3, 7, 14 and 28 days). The used parameters for the SMM model are reported in the fourth column of Table 1 and they were calibrated by fitting the load versus CMOD curves relevant to the age of 14 days. The other curves represent pure predictions of the models and show a good agreement with the experimental data.

6.5. Early age analysis of concrete wall

In this last numerical example, the computational model has been applied for the analysis of a concrete wall subjected to drying and restrained at the base by a non-shrinking foundation during the first month after the casting. This choice is motivated by the widespread occurrence of unsightly and serviceability-impairing cracks in concrete walls, which are caused by external restraint. The focus is on a qualitative study to show how numerical analyses can provide insight into the wall response. In particular, the ability of the numerical model to capture the initiation and time-dependent propagation of the primary and secondary cracks realistically is investigated. A typical normal medium strength concrete is used in this example with standard values of the parameters, which, for the sake of completeness, are reported in the last column of Table 1.

The wall shown in Fig. 12a is first analyzed for the chemo–hygro–thermal problem, in which, assuming a long wall, only the transversal section has been modeled as shown in Fig. 12b, using two-dimensional finite triangular elements, 3-node with linear shape function. The boundary conditions are influenced by the presence of the formworks, so, as a simplification, it is assumed that the formwork wall consists of 5-cm-thick wooden plates and they are removed after 28 days. In the numerical simulation they are modeled through an addition layer of material. For the humidity it is assumed a sealed condition for the first 24 h and, then, an external relative humidity of 50%; for the temperature a constant external temperature of 5 °C (278 K). Fig. 13 presents the results of the evolution of relative humidity (a) and of temperature (b) at different days. As it can be seen from Fig. 13a, the relative humidity reduces mainly due to self desiccation, whereas the reduction due to the drying is limited on the areas close to the external surface. In addition, Fig. 13b shows the evolution of the temperature that, first, increases for the hydration degree up to about 24 °C (297 K) and, than, reduces reaching the thermal equilibrium with the external temperature. Evolution of the material properties of the concrete used in this example are reported in Table 3.

The results of the CTH analysis were then used as input for the subsequent mechanical analysis, in which, exploiting the symmetry of the geometry, just 1/4 of the wall was modeled as showed in Fig. 12c. The computational domain was discretized by using three-dimensional 8-node-brick finite elements. To simulate the worst case of restraint to the shrinking wall, no slip between the foundation and the wall was considered, by assuming fixed wall base. Fig. 14 presents the results of the evolution of the maximum principal inelastic strain and of the maximum principal stress. As one can see, the model predicts a realistic crack pattern in agreement with cracking observed in concrete walls. This includes spaced vertical cracks which further develops into secondary inclined cracks.

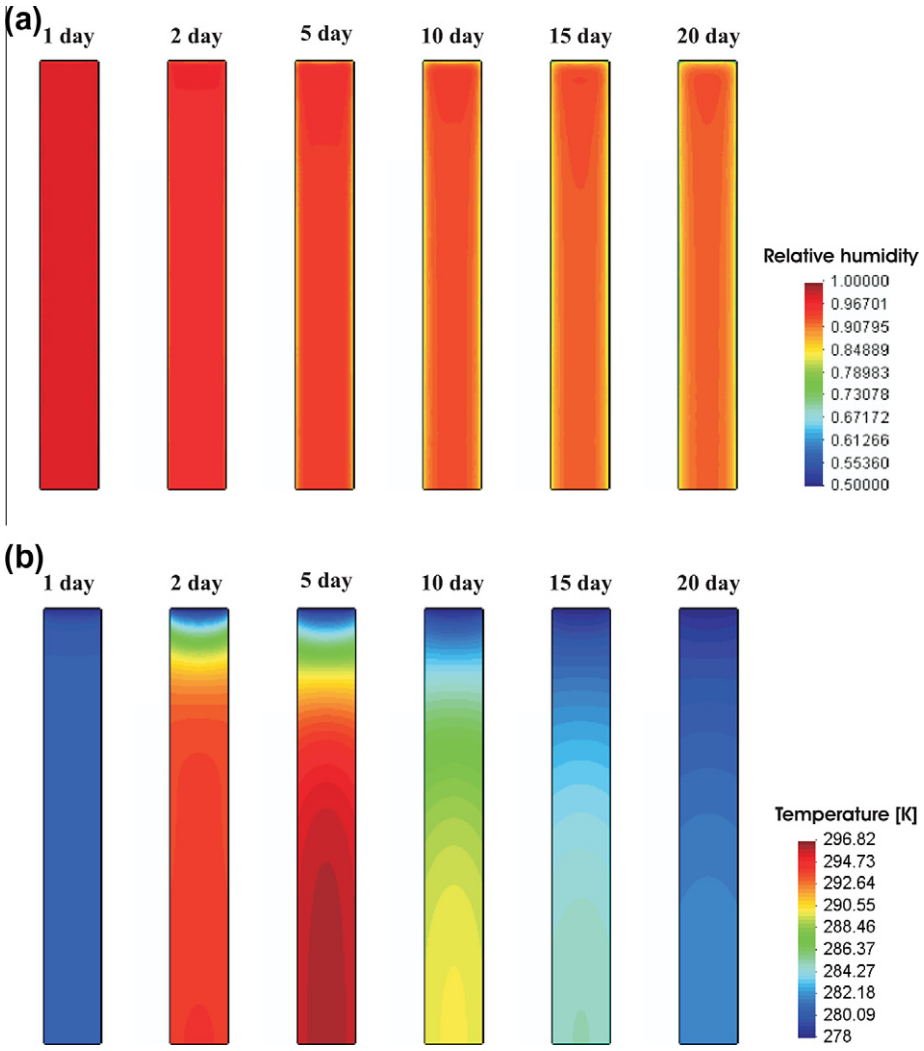

Fig. 13. Relative humidity (a) and temperature (b) in the concrete wall during the first days after casting.

Table 3
Evolution of the material properties of the concrete used in the wall example.

Age [days]	f_c [MPa]	f_t [MPa]	E [GPa]	Auto-shrink. [μm/m]	Total-shrink. (50% RH) [μm/m]	Drying creep t_0 =7 days (50% RH and 17.5 MPa) [μm/m]
3	26.80	2.04	–	37.1	102	905
7	32.20	2.53	28.176	51.2	156	1015
28	42.60	3.46	30.820	92.9	333	1255
60	–	–	–	145.4	417	1432

7. Conclusions

This paper describes a mechanical model that accounts for all the most important features observed in the behavior of concrete at early ages. The formulation is based on the coupling and amalgamation of the CTH computational framework previously developed by the authors and the formulation of a constitutive equation, entitled solidification–microprestress–microplane (SMM) model, which was obtained by extending the microplane model to include early age effects and by coupling it with the microprestress–solidification theory.

On the basis of the numerical simulations carried out in this study the following conclusions can be drawn.

1. The proposed computational framework provides a consistent approach for the simulation of aging through the adoption of the reaction degree as the main variable driving the evolution of the mechanical and hygro–thermal properties of young concrete.
2. This aging approach, although currently developed with reference to hydration and silica-fume reaction, can be easily extended to include the effect of constituents such as slag cement and fly ash.
3. The developed model can simulate with excellent accuracy aging phenomena affecting creep, strength, and fracturing behavior during self-desiccation, self heating, as well as drying of concrete at early age and beyond.

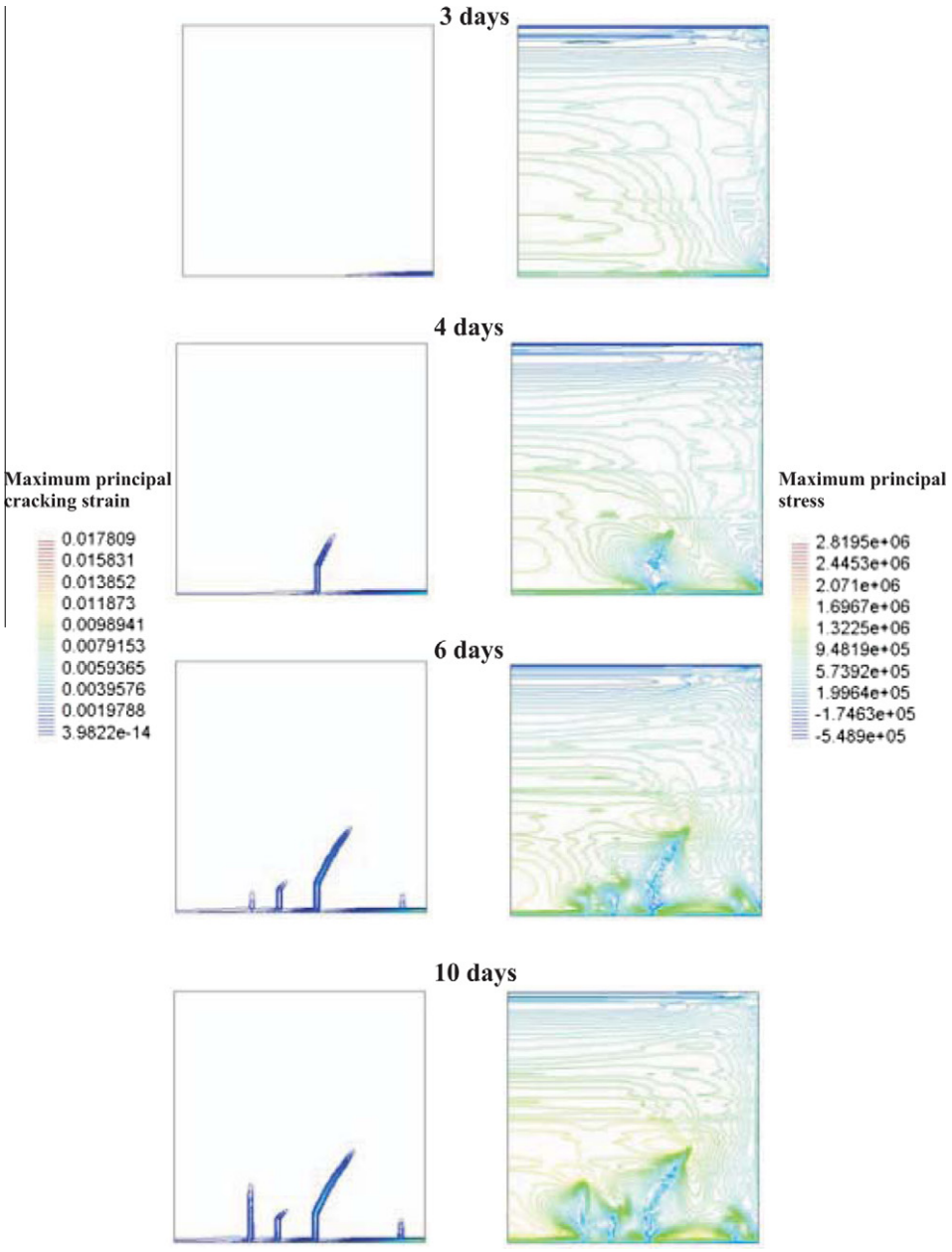

Fig. 14. Cracking strain and tensile stress in the concrete wall during the first days after casting.

Table 4
Values of the constants for each Kelvin unit in the case of $q_2 = 1$.

μ	A_μ [Pa^{-1}]	τ_μ [day]	E_μ [MPa]	η_μ [MPa day]
0	0.279	$\to 0$	–	–
1	0.053514883828698	10^{-5}	18.6863902	$5.35148838287 \times 10^{-7}$
2	0.063574529873685	10^{-4}	15.7295697	$6.35745298737 \times 10^{-6}$
3	0.074728361413693	10^{-3}	13.3818002	$7.47283614137 \times 10^{-5}$
4	0.086822042673086	10^{-2}	11.5178124	$8.68220426731 \times 10^{-4}$
5	0.099620755739032	10^{-1}	10.0380688	$9.96207557390 \times 10^{-3}$
6	0.112822584730489	1	8.86347359	0.112822584730489
7	0.126084720427353	10^{+1}	7.93117514	1.26084720427353
8	0.139058184120668	10^{+2}	7.19123442	13.9058184120668
9	0.151423850854584	10^{+3}	6.60397945	151.423850854584
10	0.162922101203790	10^{+4}	6.13790267	1629.22101203790

4. The numerical implementation of the formulated theory in standard finite element solvers is straightforward and computationally very effective.
5. The combination of the CTH and SMM models can be used confidently to solve problems of practical relevance in civil engineering.
6. To extend the range of applicability of the model, future developments of the model should include a two-way coupling between the mechanical problem and the hygro–thermal problem.

Acknowledgments

This material is based upon work supported by the Science & Technology Directorate, U.S. Department of Homeland Security,

under Award Number 2009-ST-108-001. The views and conclusions contained in this document are those of the authors and should not be interpreted as necessarily representing the official policies, either expressed or implied, of the U.S. Department of Homeland Security. In addition the authors wish to thank the graduate students Cristina Buffa, Stefano Eccheli and Mario Roveda for their contribution to the numerical simulations.

Appendix A. Microplane model constitutive equations

In this section the microplane constitutive equations used in this study are reported. In the following the superscripts "+" and "−" indicate upper bounds and lower bounds for the different measure of stress, respectively.

Normal boundaries

$$F_N^+ = \bar{E}k_1k_6c_1\exp\left(-\frac{\langle\epsilon_N - k_1k_6c_1c_2\rangle}{k_1k_5k_6c_3 + \langle -c_4\sigma_V/\bar{E}_V\rangle}\right)$$
$$F_N^- = \begin{cases} 0 & \text{for } \epsilon_N > 0 \\ -\infty & \text{for } \epsilon_N < 0 \end{cases} \tag{22}$$

where $\langle x\rangle = \max(x,0)$, $\bar{E}_V = \bar{E}/(1-2\nu)$; $c_1 = 0.5$; $c_2 = 0.45$; $c_3 = 3.75$; and $c_4 = 2.5$.

Deviatoric boundaries

$$F_D^+ = \bar{E}k_1c_5\left[1 + \left\langle\frac{\epsilon_D - k_1c_5c_6}{k_1k_5k_7c_{20}}\right\rangle^2\right]^{-1}$$
$$F_D^- = -\bar{E}k_1c_8\left[1 + \left\langle\frac{-\epsilon_D - k_1c_8c_9}{k_1k_5k_7}\right\rangle^2\right]^{-1} \tag{23}$$

where $\epsilon_D = \epsilon_N - \epsilon_V$ is the deviatoric component of the normal strain; $\epsilon_V = \epsilon_{ii}/3$ is the volumetric strain; $c_5 = 2.3$; $c_6 = 2.2$; $c_8 = 4.9$; $c_9 = 0.75$; and $c_{20} = 0.05$.

Volumetric boundary

$$F_V^- = -\bar{E}k_1k_3\exp\left[-\epsilon_V/(k_1k_4)\right] \tag{24}$$

Shear boundary

$$F_T = \frac{\bar{E}_Tk_1k_2c_{10}\langle -\sigma_N + \sigma_N^0\rangle}{\bar{E}_Tk_1k_2 + c_{10}\langle -\sigma_N + \sigma_N^0\rangle}; \quad \sigma_N^0 = \bar{\sigma}_N^0\exp\left(-\frac{\langle\epsilon_I - \epsilon_I^0\rangle}{c_{12}k_5}\right) \tag{25}$$

where $\bar{E}_T = \bar{E}/(1+\nu)$; $\bar{\sigma}_N^0 = \bar{E}_Tk_1k_6c_{11}$; ϵ_I = maximum principal strain; $\epsilon_I^0 = k_1k_6c_{21}$; $c_{10} = 0.75$; $c_{11} = 0.95$; $c_{12} = 0.02$; $c_{21} = 0.51$.

Transition function

$$\varphi = 1 - \exp\left(-c_{15}\sin\left[\frac{\pi}{2}\min\left(\langle\sigma_I + \sigma_{I0}\rangle\sigma_{I0}^{-1}; 1\right)\right]\langle\epsilon_V - \epsilon_{V0}\rangle\epsilon_{V0}^{-1}\right) \tag{26}$$

if $\epsilon_{III} > -\epsilon_{III0}$; and $\varphi = 0$ if $\epsilon_{III} \leqslant -\epsilon_{III0}$; where σ_I = maximum principal stress; ϵ_{III} = minimum principal strain; $\sigma_{I0} = \bar{E}k_1k_6c_{13}$; $\epsilon_{V0} = k_1k_6c_{14}$; $\epsilon_{III0} = k_1k_6c_{19}$; $c_{13} = 0.05$; $c_{14} = c_{15} = 0.5$; and $c_{19} = 6.06$.

The transition function is used to compute the normal microplane stress as $\sigma_N = \varphi\sigma_N^{\text{no split}} + (1-\varphi)\sigma_N^{\text{split}}$ where $\sigma_N^{\text{no split}}$ and σ_N^{split} are the normal microplane stresses obtained from the no-split formulation and the vol-dev split formulation. For additional details see Di Luzio (2007).

Appendix B. Moisture permeability and evaporable water

Following Di Luzio and Cusatis (2009a), the moisture permeability is assumed to be a nonlinear function of the relative humidity h and temperature T is formulated as follows

$$D_h(h,T) = \exp\left(\frac{E_{ad}/R}{T_0 - T}\right)D_1\left[1 + \left(\frac{D_1}{D_0} - 1\right)(1-h)^n\right]^{-1} \tag{27}$$

where $T_0 = 296$ K, $E_{ad}/R \approx 2700$ K (Bažant, 1972).

The evaporable water – sorption/desorption isotherm – can be assumed to be a function of relative humidity, degree of hydration, and degree of silica fume reaction (Norling Mjonell, 1997):

$$w_e(h,\alpha_c,\alpha_s) = G_1(\alpha_c,\alpha_s)\left[1 - \frac{1}{e^{10(g_1\alpha_c^\infty - \alpha_c)h}}\right] + K_1(\alpha_c,\alpha_s)\left[e^{10(g_1\alpha_c^\infty - \alpha_c)h} - 1\right] \tag{28}$$

$$G_1(\alpha_c,\alpha_s) = k_{vg}^c\alpha_c c + k_{vg}^s\alpha_s s \tag{29}$$

$$K_1(\alpha_c,\alpha_s) = \frac{w_0 - 0.188\alpha_c c + 0.22\alpha_s s - G_1\left[1 - e^{-10(g_1\alpha_c^\infty - \alpha_c)}\right]}{e^{10(g_1\alpha_c^\infty - \alpha_c)} - 1} \tag{30}$$

where g_1; k_{vg}^c; and k_{vg}^s are material parameters.

Appendix C. Numerical integration of creep constitutive equations

The non-aging microcompliance function is approximated through a Dirichlet series (Bažant and Prasannan, 1989a)

$$\Phi(t - t_0) \approx A_0 + \sum_{\mu=1}^{N}A_\mu\left[1 - \exp\left(-\frac{t - t_0}{\tau_\mu}\right)\right] \tag{31}$$

where $A_\mu = \ln(10)L(\tau_\mu)$; $\tau_\mu = 10\tau_{\mu-1}$ $(\mu = 1,2,\ldots,N)$; and $L(\tau_\mu)$ is the continuous relaxation spectrum of the non-aging micro-compliance function (Bažant and Xi, 1995). In this study $N = 10$ was used and the compliances A_μ, elastic moduli $E_\mu = 1/A_\mu$, and viscosity $\eta_\mu = \tau_\mu E_\mu$ are reported in Table 4 in the case of $q_2 = 1$. The strain in the individual Kelvin unit $\boldsymbol{\gamma}_\mu(t)$ reads

$$\boldsymbol{\gamma}_\mu(t_n) = \boldsymbol{\gamma}_\mu(t_{n-1})e^{-\Delta t_{n-1}/\tau_\mu} + A_\mu\left(1 - e^{-\Delta t_{n-1}/\tau_\mu}\right)\boldsymbol{\sigma}_{n-1} + A_\mu\left(1 - \frac{1 - e^{-\Delta t_{n-1}/\tau_\mu}}{\Delta t_{n-1}/\tau_\mu}\right)\Delta\boldsymbol{\sigma}_{n-1} \tag{32}$$

where $\Delta\boldsymbol{\sigma}_{n-1} = \boldsymbol{\sigma}_n - \boldsymbol{\sigma}_{n-1}$; $\Delta t_{n-1} = t_n - t_{n-1}$. The visco-elastic compliance and the imposed visco-elastic strains increments read

$$C_n^v = v(\alpha_{n+1/2})\left[A_0 + \sum_{\mu=1}^{N}A_\mu\left(1 - \frac{1 - e^{\Delta t_n/\tau_\mu}}{\Delta t_n/\tau_\mu}\right)\right] \tag{33}$$

and

$$\Delta\boldsymbol{\epsilon}_n^{v'''} = v(\alpha_{n+1/2})\left[\sum_{\mu=1}^{N}(1 - e^{-\Delta t_n/\tau_\mu})\left(A_\mu\boldsymbol{\sigma}_n - \boldsymbol{\gamma}_\mu(t_n)\right)\right] \tag{34}$$

The purely viscous strain component can be integrated by the central difference approximation giving the viscous compliance and imposed strains as $C_n^f = 0.5q_4\kappa_0S(t_{n+1/2})\psi(t_{n+1/2})\Delta t_n$ and $\Delta\boldsymbol{\epsilon}_n^{f''} = q_4\kappa_0S(t_{n+1/2})\psi(t_{n+1/2})\mathbf{G}\boldsymbol{\sigma}_n$. The value of the microprestress at time $t_{n+1/2}$ can be computed as $S(t_{n+1/2}) = S(t_n) + \Delta S_n/2$ and

$$\Delta S_n = -\kappa_0\omega(t_{n+1/2})\Delta t_nS(t_{n+1/2})^2 + \kappa_1\left|\Delta T\ln h(t_{n+1/2}) + T(t_{n+1/2})\frac{\Delta h}{h(t_{n+1/2})}\right| \tag{35}$$

which needs to be solved iteratively within each time step.

References

Baroghel-Bouny, V., Mainguya, M., Lassabatereb, T., Coussya, O., 1999. Characterization and identification of equilibrium and transfer moisture properties for ordinary and high-performance cementitious materials. Cement and Concrete Research 29, 1225–1238.

Bažant, Z., Planas, J., 1997. Fracture and Size Effect in Concrete and Other Quasibrittle Materials. In: Chen, W.F. (Ed.), . New Directions in Civil Engineering. CRC Press.
Bažant, Z.P., 1972. Thermodynamics of interacting continua with surfaces and creep analysis of concrete structures. Nuclear Engineering and Design 20, 477–505.
Bazant, M.Z., Bazant, Z.P., 2012a. Theory of sorption hysteresis in nanoporous solids: II. Molecular condensation. Journal of the Mechanics and Physics of Solids 60, 1660–1675.
Bazant, Z.P, Bazant, M.Z., 2012b. Theory of sorption hysteresis in nanoporous solids: I. Snap through instabilities. Journal of the Mechanics and Physics of Solids 60, 1644–1659.
Bažant, Z.P., Baweja, S., 1995. Creep and shrinkage prediction model for analysis and design of concrete structures—Model B3. Materials and Structures 28, 357–365.
Bažant, Z.P., Caner, F.C., 2005. Microplane model M5 with kinematic and static constraints for concrete fracture and anelasticity. I: theory. Journal of Engineering Mechanics, ASCE 131 (1), 31–40.
Bažant, Z.P., Caner, F.C., Carol, I., Adley, M.D., Akers, S.A., 2000. Microplane model M4 for concrete. I: formulation with work-conjugate deviatoric stress. Journal of Engineering Mechanics, ASCE 126 (9), 944–953.
Bažant, Z.P., Cusatis, G., Cedolin, L., 2004. Temperature effect on concrete creep modeled by microprestress–solidification theory. Journal of Engineering Mechanics 130 (6), 691–699.
Bažant, Z.P., Di Luzio, G., 2004. Nonlocal microplane model with strain-softening yield limits. International Journal of Solids and Structures 41 (24–25), 7209–7240.
Bažant, Z.P., Gambarova, P., 1984. Crack shear in concrete: crack band microplane model. Journal of Engineering Mechanics, ASCE 110, 2015–2035.
Bažant, Z.P., Hauggaard, A.B., Baweja, S., Ulm, F.J., 1997a. Microprestress–solidification theory for concrete creep. I: aging and drying effects. Journal of Engineering Mechanics, ASCE 123, 1188–1194.
Bažant, Z.P., Hauggaard, A.B., Baweja, S., 1997b. Microprestress–solidification theory for concrete creep. II: algorithm and verification. Journal of Engineering Mechanics, ASCE 123, 1195–1201.
Bažant, Z.P., Najjar, L.J., 1972. Nonlinear water diffusion in nonsaturated concrete. Materials and Structures 5, 3–20.
Bažant, Z.P., Oh, B.H., 1983. Crack band theory for fracture of concrete. Matériaux et Constructions 16, 155–177.
Bažant, Z.P., Prasannan, S., 1989a. Solidification theory for concrete creep. I: formulation. Journal of Engineering Mechanics, ASCE 115, 1691–1703.
Bažant, Z.P., Prasannan, S., 1989b. Solidification theory for concrete creep. II: verification and application. Journal of Engineering Mechanics, ASCE 115, 1704–1725.
Bažant, Z.P., Xi, Y., 1995. Continuous retardation spectrum for solidification theory of concrete creeps. Journal of Engineering Mechanics, ASCE 121, 281–288.
Belytschko, T., Liu, W.K., Moran, B., 2000. Nonlinear Finite Elements for Continua and Structures. Wiley, Chichester, England.
Bryant, A.H., Vadhanavikkit, C., 1987. Creep, shrinkage size, and age at loading effects. ACI Materials Journal 84 (2), 117–123.
Carino, N.J., 1981. Temperature effects on the strength–maturity relation of mortar. Struc. Res. Lab. Rep. NBSSIR 81-2244, National Bureau of Standards, Washington, DC.
Carol, I., Jirásek, M., Bažant, Z.P., 2001. A thermodynamically consistent approach to microplane theory. Part I: free energy and consistent microplane stresses. International Journal of Solids and Structures 38 (17), 2921–2931.
Cervera, M., Oliver, J., Prato, T., 1999a. Thermo–chemo–mechanical model for concrete. I: hydration and aging. Journal of Engineering Mechanics, ASCE 125 (9), 1018–1027.
Cervera, M., Oliver, J., Prato, T., 1999b. Thermo–chemo–mechanical model for concrete. II: damage and creep. Journal of Engineering Mechanics, ASCE 125 (9), 1028–1039.
Cusatis, G., Beghini, A., Bažant, Z., 2008. Spectral stiffness microplane model for quasi-brittle composite laminates: I. Theory. Journal of Applied Mechanics, ASME 75 (1), 021009-1–021009-9.
Cusson, D., Hoogeveen, T., 2007. An experimental approach for the analysis of early-age behaviour of high-performance concrete structures under restrained shrinkage. Cement and Concrete Research 37, 200–209.
de Schutter, G., Taerwe, L., 1995. General hydration model for portland cement and blast furnace slag cement. Cement and Concrete Research 25 (3), 593–604.
de Schutter, G., Taerwe, L., 1996. Degree of hydration based description of mechanical properties of early age concrete. Materials and Structures 29, 335–344.
Di Luzio, G., 2007. A symmetric over-nonlocal microplane model m4 for fracture in concrete. International Journal of Solids and Structures 44 (13), 4418–4441.
Di Luzio, G., 2009. Numerical model for time-dependent fracturing of concrete. Journal of Engineering Mechanics, ASCE 135 (7), 632–640.
Di Luzio, G., Bažant, Z.P., 2005. Spectral analysis of localization in nonlocal and over-nonlocal materials with softening plasticity or damage. International Journal of Solids and Structures 42 (23), 6071–6100.
Di Luzio, G., Cusatis, G., 2009a. Hygro–thermo–chemical modeling of high performance concrete. I: theory. Cement and Concrete Composites 31 (5), 301–308.
Di Luzio, G., Cusatis, G., 2009b. Hygro–thermo–chemical modeling of high performance concrete. II: numerical implementation, calibration, and validation. Cement and Concrete Composites 31 (5), 309–324.
Di Luzio, G., Cusatis, G., 2012. Calibration and validation of a numerical model for early age damage analysis. In: Carrato, J., Burns, J. (Eds.), Structures Congress – 20th Analysis & Computation Specialty Conference – ASCE, vol. 1. American Society of Civil Engineers (ASCE), Chicago, IL, USA, pp. 437–448.
Di Luzio, G., Cusatis, G., Cedolin, L., 2010a. A numerical model for early age concrete behavior. In: Bicanic, N., Borst, R., Mang, H., Meschke, G. (Eds.), Conference on Computational Modelling of Concrete Structures – EURO-C 2010, vol. 1. CRC Press, London, UK, pp. 481–486.
Di Luzio, G., Muciaccia, G., Biolzi, L., 2010b. Size effect in thermally damaged concrete. International Journal of Damage Mechanics 19 (5), 631–656.
di Prisco, M., Colombo, M., Ferrara, L., Bamonte, P., Bencardino, F., Dozio, D., Galeota, D., Galli, G., Gambarova, P., Gianmatteo, M.M., Gregori, A., Grimaldi, A., Marino, R., Rinaldi, R., Rizzuti, L., Spadea, G., 2007. Fibre Reinforced Concrete for Strong, Durable and Cost-Saving Structures and Infrastructures. Starrylink, Brescia, Italy, pp. 9–36 (FRC and HPFRC material properties).
Feldman, R.F., 1968. Sorption and length-change scanning isotherms of methanol and water on hydrated Portland cement. In: Proceedings of the 5th International Congress on the Chemistry of Cement, pp. 53–66.
Gawin, D., Pesavento, F., Schrefler, B.A., 2006a. Hygro–thermo–chemo–mechanical modelling of concrete at early ages and beyond. Part I: hydration and hygro–thermal phenomena. International Journal for Numerical Methods in Engineering 67 (3), 299–331.
Gawin, D., Pesavento, F., Schrefler, B.A., 2006b. Hygro–thermo–chemo–mechanical modelling of concrete at early ages and beyond. Part II: shrinkage and creep of concrete. International Journal for Numerical Methods in Engineering 67 (3), 332–363.
Hillerborg, A., 1985. The theoretical basis of a method to determine the fracture energy of concrete. Materials and Structures 18, 291–296.
Jirásek, M., Bažant, Z.P., 2002. Inelastic Analysis of Structures. John Wiley and Sons, London, New York.
Khan, A.A., Cook, W.D., Mitchell, D., 1995. Early age compressive stress–strain properties of low-medium, and high-strength concretes. ACI Materials Journal 92 (6), 617–624.
Khan, A.A., Cook, W.D., Mitchell, D., 1997. Creep, shrinkage, and thermal strains in normal, medium, and high-strength concretes during hydration. ACI Materials Journal 94 (2), 156–163.
Kim, J.-K., Han, S.H., Song, Y.C., 2002. Effect of temperature and aging on the mechanical properties of concrete: Part I. Experimental results. Cement and Concrete Research 32 (7), 1087–1094.
Kim, J.-K., Lee, Y., Yi, S.-T., 2004. Fracture characteristics of concrete at early ages. Cement and Concrete Research 34 (3), 507–519.
Kim, J.-K., Moon, Y.-H., Eo, S.-H., 1998. Compressive strength development of concrete with different curing time and temperature. Cement and Concrete Research 28 (12), 1761–1773.
Kjellsen, K.O., Detwiler, R.J., 1998. Later-age strength prediction by a modified maturity model. Material Journal, ACI 90 (3), 220–227.
Lackner, R., Mang, H.A., 2004. Chemoplastic material model for the simulation of early-age cracking: from the constitutive law to numerical analyses of massive concrete structures. Cement and Concrete Composites 26 (5), 551–562.
Laplante, P., 1993. Mechanical properties of hardening concrete: a comparative analysis of classical and high strength concretes. Ph.D. thesis, Ecole Nationale des Ponts et Chaussées, Paris (in French).
L'Hermite, R., Mamillan, M., Lefèvre, C., 1965. Nouveaux résultats de recherches sur la déformation et la rupture du béton. Supplément aux annales de l'istitut technique du bâtiment et des travaux publics 207/208, 325–345 (in French).
Neville, A., 1997. Properties of Concrete. John Wiley and Sons, New York.
Norling Mjonell, K., 1997. A model on self-desiccation in high-performance concrete. In: Self-desiccation and Its Importance in Concrete Technology. Proceedings of the International Research Seminar, Lund, Sweden, pp. 141–157.
Oluokun, F., 1991. Prediction of concrete tensile strength from its compressive strength: an evaluation of existing relations for normal weight concrete. Materials Journal – ACI 88 (3), 302–309.
Oluokun, F.A., Burdette, E.G., Deatherage, J.H., 1991. Splitting tensile strength and compressive strength relationships at early ages. Materials Journal – ACI 88 (2), 115–121.
Ožbolt, J., Li, Y., Kožar, I., 2001. Microplane model for concrete with relaxed kinematic constraint. International Journal of Solids and Structures 38 (16), 2683–2711.
Petersson, P.E., 1980. Fracture energy of concrete: practical performance and experimental results. Cement and Concrete Research 10, 91–101.
RILEM Committee TC-69, 1988. Material models for structural creep analysis (princ. author Z.P. Bazant). In: Bazant, Z.P. (Ed.), Mathematical Modeling of Creep and Shrinkage of Concrete, J. Wiley, Chichester, New York, pp. 99–200 (Chapter 2).
Ulm, F.J., Coussy, O., 1995. Modeling of thermochemomechanical couplings of concrete at early ages. Journal of Engineering Mechanics, ASCE 121 (7), 785–794.
Ulm, F.J., Coussy, O., 1996. Strength growth as chemo–plastic hardening in early age concrete. Journal of Engineering Mechanics, ASCE 122 (12), 1123–1132.
Verbeck, G.J., Helmuth, R.H., 1968. Bonded anchors in high performance fibre reinforced concrete. In: 5th Int. Symp. on the Chemistry of Cement, pp. 1–32.
Wittmann, F.H., 1982. Creep and shrinkage mechanics. In: Bažant, Z.P., Wittmann, F.H. (Eds.), Creep and Shrinkage of Concrete Structures. John Wiley & Sons Ltd., pp. 129–161 (Chapter 6).
Wittmann, F.H., Beltzung, F., Zhao, T.-J., 2009. Shrinkage mechanisms, crack formation and service life of reinforced concrete structures. International Journal of Structural Engineering 1 (1), 13–28.